5-2018

Synthesis of Inhomogeneous Waves Using the Least-Squares Method

Trevor A. Kyle
Purdue University

SYNTHESIS OF INHOMOGENEOUS WAVES USING THE LEAST-SQUARES METHOD

A Thesis

Submitted to the Faculty

of

Purdue University

by

Trevor A. Kyle

In Partial Fulfillment of the

Requirements for the Degree

of

Master of Science in Mechanical Engineering

May 2018

Purdue University

West Lafayette, Indiana

THE PURDUE UNIVERSITY GRADUATE SCHOOL STATEMENT OF COMMITTEE APPROVAL

Dr. Jeffrey F. Rhoads, Co-Chair

School of Mechanical Engineering

Dr. J. Stuart Bolton, Co-Chair

School of Mechanical Engineering

Dr. Fabio Semperlotti

School of Mechanical Engineering

Approved by:

Dr. Jay P. Gore

Associate Head for Graduate Studies

ACKNOWLEDGMENTS

I would like to thank Dr. Rhoads and Dr. Bolton for giving me their support and for taking the risk of adding a nuclear engineer to their team. I would also like to express my gratitude to Dr. Daniel Woods for providing the background and framework for my research, Caleb Heitkamp for working in parallel with me and providing samples, and Sam Wonfor for running countless tests over the summer. Finally, I would like to thank Schuyler Putt, without whose influence I never would have gone to graduate school to study acoustics and vibrations.

This research is supported by Purdue University, as well as by the United States Department of Defense, Office of Naval Research through grant No. N00014-16-1-2275. The content of the information does not necessarily reflect the position or the policy of the U.S. federal government, and no official endorsement should be inferred.

TABLE OF CONTENTS

LIST OF TABLES

LIST OF FIGURES

Figure Page

Figure Page

Figure Page

Figure Page

ABSTRACT

Kyle, Trevor A. M.S.M.E., Purdue University, May 2018. Synthesis of Inhomogeneous Waves Using the Least-Squares Method. Major Professors: Jeffrey F. Rhoads and J. Stuart Bolton, School of Mechanical Engineering.

The aim of the work presented in this document is to demonstrate the versatility and applicability of least-squares reconstruction of acoustic waves. Appropriately tailored, certain kinds of acoustic waves are able to thermomechanically excite energetic materials in a safe, reliable manner. This allows for easier and more effective detection than current methods are able to offer.

Typically, due to the large impedance difference between any given fluid and solid, it is exceedingly difficult to transmit energy between the two dissimilar media. However, it has been shown that certain spatially decaying plane waves, called inhomogeneous waves, are able to breach the fluid–solid barrier and transfer most of their energy into the second medium. However, as inhomogeneous acoustic waves cannot be easily generated from a single source, they must be reconstructed as a superposition of several waves from independent sources. This approach was studied through the lens of the least-squares method, which tunes a discrete number of sources to produce a desired waveform on a target surface. The simulations presented in this document analyze the range of parameters for which the least-squares method of sound field reconstruction provides an acceptable and physically feasible output.

The conditions of these simulations were tested with real sources to determine the extent to which irregularities in the sources affected the reconstruction accuracy. By constructing an array of sources and an array of receivers, the effects of varying the standoff distance, source spacing, and level of inhomogeneity were analyzed. While empirical adjustments to the established model were not able to reduce the recon-

struction error to the theoretical levels, they did allow for accurate reconstruction over a wide range of excitation parameters.

This document provides the framework for further tests of least-squares reconstruction over a wide span of parameters. Utilizing the methods discussed here, progress can be made towards the eventual goal of inducing a temperature increase in a mock energetic material utilizing inhomogeneous acoustic waves.

1. INTRODUCTION

Portions of this chapter have been adapted from Kyle et al.: "Least-squares reconstruction of low-frequency inhomogeneous plane waves" [1].

1.1 Background and Motivation

The ability to determine a material's chemical properties is in the interest of numerous industries, both to ensure quality products and to detect potentially harmful substances. A chemical signature can provide significant insight into the characteristics of a material, ranging from tensile and compressive strength [2] to acidity [3]. Of particular interest is the ability to positively identify energetic materials, substances that are able to detonate or deflagrate under certain conditions. These materials are used in the creation of improvised explosive devices (IEDs), which often contain energetic crystals suspended in a matrix of binder material [4]. IEDs pose a significant threat to both the armed forces and civilians due to their ability to be concealed or otherwise hidden, so it is critically important to be able to detect and classify them.

One of the most commonly used strategies of identifying sensitive materials, such as the explosives RDX and HMX, is trace vapor detection, which uses a sensor to analyze air with the intent of discovering very small amounts of the material that have vaporized. Trace vapor detection can be implemented through various methods, such as the use of trained animals or the sampling of air in the vicinity of a suspected energetic material [5, 6]. However, since many IEDs are obscured or contained within packaging, their vapor pressure may be too low to allow for reliable detection. It has been shown that the vapor pressure of many energetic materials is highly dependent on temperature, with even small increases in temperature leading to greatly increased concentrations of vapors. For RDX, an increase in temperature from 25 °C to 27 °C

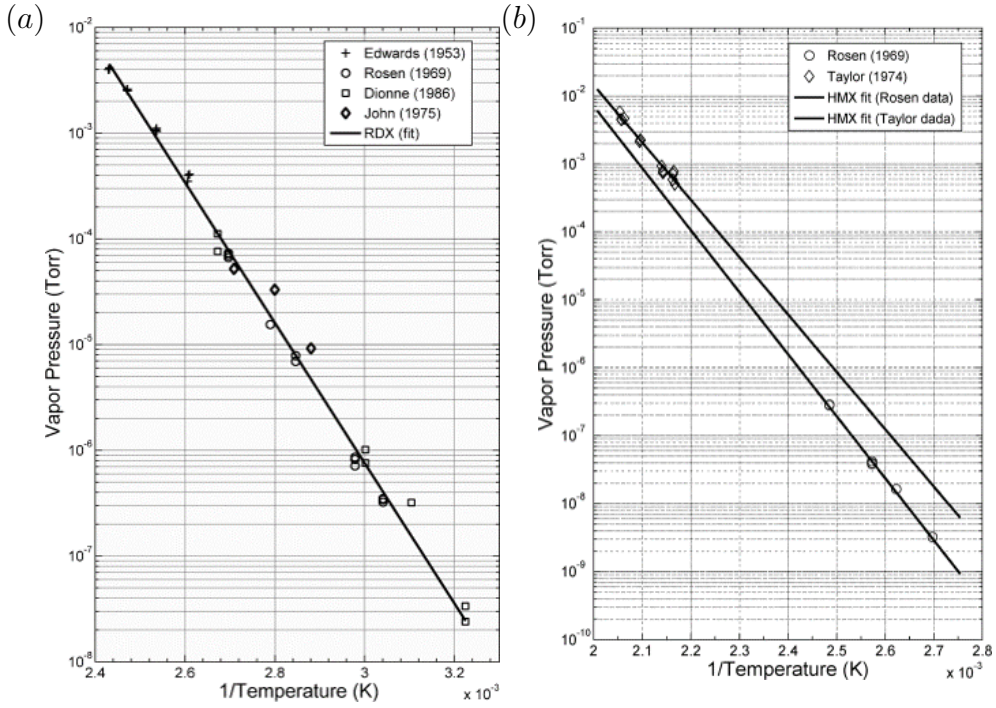

Figure 1.1. A diagram showing the relationship between vapor pressure and temperature of the explosives (a) RDX and (b) HMX, reproduced from Östmark et al. [7]

results in a 40% increase in vapor pressure [7]. For HMX, the same temperature change increases the pressure by 60% [7]. Fig. 1.1 shows the strong temperature dependence of these explosives' vapor pressures.

Temperature changes in materials can be induced by mechanical vibrations [8], but due to the typically concealed nature of IEDs and their unknown composition, the mechanical excitation of them is often impossible or dangerous. An alternative to mechanical excitation is acoustic excitation, which utilizes sound waves to transmit energy into the material. Because energy can be transmitted through waves, it is not necessary to be physically in contact with or even near an IED in order to interact with it and identify it. This significantly reduces the risk of inadvertently triggering a deadly reaction that could harm the investigators.

The use of acoustic waves as a method of excitation comes at a cost, however, as sound waves do not typically transmit a significant amount of energy when they are incident on a barrier or interface between two different media. This is attributable to the acoustic impedance difference between the two media, which are often a fluid (like air), and a solid (like an energetic material) [9–11]. In order to address this limitation, previous work has considered the use of incident inhomogeneous plane waves. It was demonstrated that by tuning the incidence angle and inhomogeneity, small reflection (and large energy transmission) values are predicted in the context of lossless and low-loss fluid–solid interfaces [12, 13].

By developing a method to reliably implement the type of acoustic wave necessary to transmit energy across the boundary of a medium, it will be possible to thermomechanically excite energetic materials, which will allow for detection and identification.

The remainder of Chapter 1 describes the representation and behavior of acoutic waves. Chapter 2 provides a framework that models the reconstructed sound field at any point in space as a function of source inputs. Chapter 3 explores various methods of characterizing real sources and compares theoretical and experimental results. Chapter 4 draws pertinent conclusions and provides a basis for future work, which includes the first steps in connecting the reconstruction of sound fields with the excitation of mock energetic materials.

1.2 Representation of Acoustic Waves

Materials or fluids that are homogeneous and isotropic have a uniform composition and bulk properties that are independent of direction. A harmonic plane wave propagating in a homogeneous, isotropic, fluid can be represented by the complex pressure as [9, 14]:

$$\tilde{p} = \tilde{p}_0 \mathrm{e}^{\mathrm{i}(\omega t - \tilde{\mathbf{K}} \cdot \mathbf{r})}, \tag{1.1}$$

where $\tilde{p}_0$ denotes the complex pressure amplitude, i is the imaginary unit, ω denotes the angular frequency, t denotes the time variable, $\tilde{\mathbf{K}}$ is the complex wavevector,

and $\mathbf{r}$ is the position vector. The wavevector must satisfy the material wavenumber condition in the fluid [14], i.e.,

$$\tilde{\mathbf{K}} \cdot \tilde{\mathbf{K}} = \tilde{k}^2, \tag{1.2}$$

where $\tilde{k}$ is the material wavenumber for longitudinal waves. If the fluid is assumed to be lossless, which is a good approximation for air in the low-frequency regime, then the material wavenumber is simply $k = \omega/v$, where v is the longitudinal wave speed. In that case, for the plane wave under consideration, the planes of constant amplitude must be perpendicular to the planes of constant phase.

By expanding the wavevector into its scalar components and assuming that the wave is traveling at an angle θ with respect to a coordinate system, Eq. (1.1) can be written as

$$\tilde{p} = \tilde{p}_0 \mathrm{e}^{\mathrm{i}(\omega t - k\cos\theta z - k\sin\theta x)} \tag{1.3}$$

This type of wave is known as a homogeneous plane wave, as its amplitude is constant along a line perpendicular to its propagation vector. In practice, very few waves are truly plane waves, although spherical waves can sometimes be approximated as plane waves if their frequency is low and they are very far away from their source.

1.2.1 Reflection and Transmission of Plane Waves

When an acoustic wave is incident on an interface between two media, the nature of the wave that propagates into the second medium and the amount of energy that it carries are highly dependent on the difference in the material properties of the media.

In the case of a homogeneous plane wave incident on a fluid–fluid boundary (e.g., air to water), the pressure field in the first medium can be represented by the superposition of the incident and reflected waves:

$$p_1 = \mathrm{e}^{\mathrm{i}(\omega t - k_1\cos\theta z - k_1\sin\theta x)} + R\mathrm{e}^{\mathrm{i}(\omega t + k_1\cos\theta_r z - k_1\sin\theta_r x)} \tag{1.4}$$

where k_1 is the material wavenumber of the first medium, θ is the angle of incidence, θ_r is the angle of reflection, and R is the pressure reflection coefficient. Because fluids cannot support shear waves, the pressure field in the second medium is simply the transmitted longitudinal wave:

$$p_2 = T\mathrm{e}^{\mathrm{i}(\omega t - k_2 \cos\theta_t z - k_2 \sin\theta_t x)} \tag{1.5}$$

where k_2 is the material wavenumber of the second medium, θ_t is the angle of transmission, and T is the pressure transmission coefficient. The fluid–fluid interface with the incident, reflected, and transmitted waves is shown in Fig. 1.2.

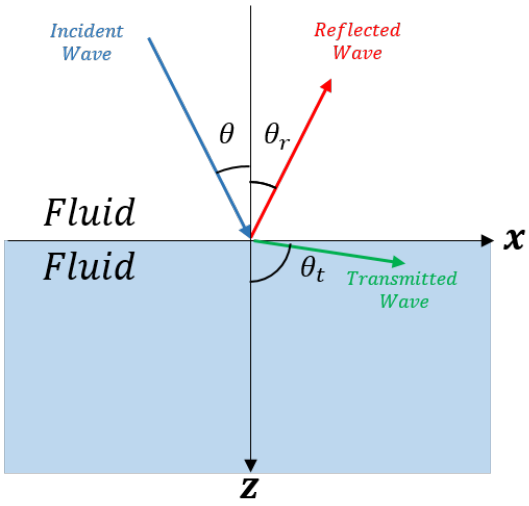

Figure 1.2. A diagram showing the interaction of a plane wave incident on a fluid–fluid boundary.

Since the pressures in each medium are equal at the interface where $z = 0$, Eqs. (1.4) and (1.5) reduce to

$$\mathrm{e}^{-\mathrm{i}k_1 \sin\theta x} + R\mathrm{e}^{-\mathrm{i}k_1 \sin\theta_r x} = T\mathrm{e}^{-\mathrm{i}k_2 \sin\theta_t x} \tag{1.6}$$

Because the pressure boundary condition is independent of x, the quantities in the exponents must be equal. By equating the first two exponents, it can be seen that $\theta_r = \theta$. By equating the first and third exponents, Snell's Law is recovered [9]:

$$\frac{\sin\theta_t}{\sin\theta} = \frac{v_2}{v_1} \tag{1.7}$$

where v_1 and v_2 represent the longitudinal wave speeds in each medium. Notably, if $v_2 > v_1$, there exists a critical angle θ_c such that any higher value of θ would lead to $\sin\theta_t$ to be greater than unity [9]. As a result, θ_t is complex and $\cos\theta_t$ is imaginary:

$$\cos\theta_t = \pm \mathrm{i}\sqrt{(v_2/v_1)^2\sin^2\theta - 1} \tag{1.8}$$

By evaluating Eq. (1.5) and Eq. (1.7) using the negative root of Eq. (1.8), it can be seen that the transmitted wave now has an amplitude that exponentially decays into the second medium but does not propagate:

$$p_2 = T\mathrm{e}^{-\zeta z}\mathrm{e}^{\mathrm{i}(\omega t - k_1 \sin\theta x)} \tag{1.9}$$

with $\zeta = k_2\sqrt{(v_2/v_1)^2\sin^2\theta - 1}$. This wave is evanescent, as it clings to the boundary but does not transmit energy into the second medium [9]. For media that have wave speeds much greater than the surrounding fluid, the critical angle is very small, meaning that there is a very small range of angles that are able to be exploited for acoustic excitation.

For all incidence angles such that $\theta < \theta_c$, the values of the pressure reflection coefficient and pressure transmission coefficient can be found by reexamining Eq. (1.6) and again noting that the exponents all must be equal. As a result, the following equality can be made:

$$1 + R = T \tag{1.10}$$

Because the component of particle velocity normal to the boundary must also be continuous across the media, the following equality can be made, noting that particle velocity is given as $u = \pm p/\rho c$:

$$\frac{\cos\theta}{\rho_1 v_1} - R\frac{\cos\theta}{\rho_1 v_1} = T\frac{\cos\theta_t}{\rho_2 v_2} \tag{1.11}$$

Solving Eqs. (1.10) and (1.11) simultaneously yields an expression for the reflection coefficient [9]:

$$R = \frac{\frac{\rho_2 v_2}{\cos\theta_t} - \frac{\rho_1 v_1}{\cos\theta}}{\frac{\rho_2 v_2}{\cos\theta_t} + \frac{\rho_1 v_1}{\cos\theta}} \tag{1.12}$$

The value of the transmission coefficient can then be found using Eq. (1.10).

As was previously stated, at values of θ greater than θ_c, the transmitted angle θ_t will be complex. As a result, the magnitude of the pressure reflection coefficient, and therefore the power reflection coefficient, is unity at large incidence angles [9].

The mechanics of transmission and reflection become more complicated when a wave is incident on a fluid–solid boundary because solids are able to sustain shear waves as well as longitudinal waves. This is shown in Fig. 1.3, which displays the incident and reflected waves, along with the two transmitted waves.

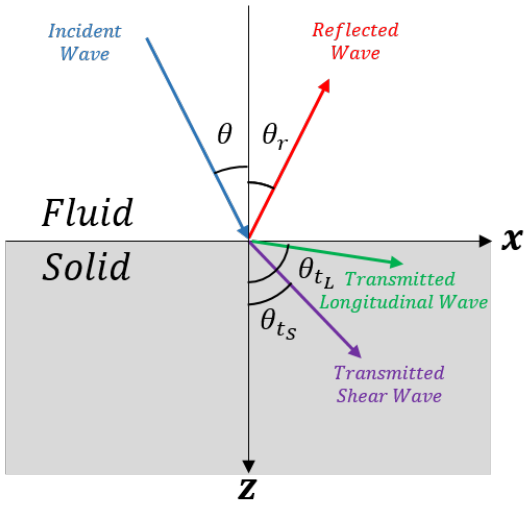

Figure 1.3. A diagram showing the interaction of a plane wave incident on a fluid–solid boundary.

The same boundary conditions of the fluid–fluid interface are maintained for a fluid–solid interface: trace wavenumber continuity, pressure/normal stress continuity,

and normal particle velocity continuity. The angle of the transmitted shear wave can be found using an expanded version of Snell's Law as

$$\frac{\sin\theta}{v_1} = \frac{\sin\theta_{t_L}}{v_{2_L}} = \frac{\sin\theta_{t_S}}{v_{2_S}} \tag{1.13}$$

where v_{2_L} is the speed of the longitudinal wave in the solid, and v_{2_S} is the speed of the shear wave in the solid. By utilizing the boundary conditions as stated, it is possible to once again solve for the pressure reflection coefficient, which Brekhovskikh reports in terms of the transmitted shear angle [10]:

$$R = \frac{\frac{\rho_2 v_{2_L}}{\cos\theta_{t_L}}\cos^2 2\theta_{2_S} + \frac{\rho_2 v_{2_S}}{\cos\theta_{t_S}}\sin^2 2\theta_{2_S} - \frac{\rho_1 v_1}{\cos\theta}}{\frac{\rho_2 v_{2_L}}{\cos\theta_{t_L}}\cos^2 2\theta_{2_S} + \frac{\rho_2 v_{2_S}}{\cos\theta_{t_S}}\sin^2 2\theta_{2_S} + \frac{\rho_1 v_1}{\cos\theta}} \tag{1.14}$$

In the context of transmitting acoustic energy from a fluid into a solid, it is desirable to minimize the magnitude of the reflection coefficient (thereby maximizing the magnitudes of the shear and longitudinal transmission coefficients). This is possible by exploiting the Rayleigh phenomenon, the condition where an incident wave perfectly excites the free wave solution of the surface. This causes the shear and longitudinal waves to travel at the same velocity along the material interface, appearing as bulk Rayleigh waves. The speed of these Rayleigh waves can be found by solving the characteristic equation and taking the positive root that is smaller than the shear wave velocity [10, 18]:

$$\left(\frac{v_{Ray}}{v_{2_S}}\right)^6 - 8\left(\frac{v_{Ray}}{v_{2_S}}\right)^4 + \left[24 - 16\left(\frac{v_{2_S}}{v_{2_L}}\right)^2\right]\left(\frac{v_{Ray}}{v_{2_S}}\right)^2 - 16\left[1 - \left(\frac{v_{2_S}}{v_{2_L}}\right)^2\right] = 0 \tag{1.15}$$

where v_{Ray} is the Rayleigh wave speed. The Rayleigh angle θ_{Ray} is then found as follows:

$$\theta_{Ray} = \arcsin\frac{v_{1_L}}{v_{Ray}} \tag{1.16}$$

While transmission would generally be optimized at the Rayleigh angle, the large impedance difference between fluids and solids often places the Rayleigh angle much

higher than the critical angle, which, as mentioned previously, leads to the total reflection of homogeneous plane waves. However, the Rayleigh phenomenon can still be exploited, and the reflection coefficient can be reduced to zero, if the incident wave takes the form of an evanescent wave, hereafter referred to as an inhomogeneous plane wave.

1.2.2 Inhomogeneous Plane Waves

In a homogeneous plane wave, the wavevector $\tilde{\mathbf{K}}$ is real, and the directional wavenumbers are simply projections of the material wavenumber onto an arbitrary coordinate system. However, for inhomogeneous plane waves, this is not the case. By writing the complex wavevector in terms of the real propagation vector $\mathbf{C}$ and real attenuation vector $\mathbf{A}$, $\tilde{\mathbf{K}} = \mathbf{C} - \mathrm{i}\mathbf{A}$; this condition is then $\mathbf{C} \perp \mathbf{A}$, where $\mathbf{A} = \mathbf{0}$ for homogeneous plane waves and $\mathbf{A} \neq \mathbf{0}$ for inhomogeneous waves. Introducing the inhomogeneity, or decay, parameter $\beta = |\mathbf{A}|$, Eq. (1.1) can be written, for two-dimensional propagation in the xz-plane:

$$\tilde{p} = \tilde{p}_0 \mathrm{e}^{-\beta[-\cos\theta x + \sin\theta z]} \mathrm{e}^{\mathrm{i}[\omega t - |\mathbf{C}|\sin\theta x - |\mathbf{C}|\cos\theta z]} \tag{1.17}$$

where the incidence angle θ and right-handed Cartesian coordinate system shown in Figs. 1.2 and 1.3 have been used, and where $|\mathbf{C}|$ is computed from Eq. (1.2).

In the context of mathematical completeness, this decay parameter can be expressed as an imaginary component of a complex incidence angle, such that $\theta = \theta_{\Re} + \mathrm{i}\theta_{\Im}$, as follows:

$$\theta_{\Im} = \pm \ln \left(\frac{|\beta|}{k} + \left[\left(\frac{\beta}{k} \right)^2 + 1 \right]^{1/2} \right) \tag{1.18}$$

This corresponds to the inversion of $\beta = k \sinh \theta_{\Im}$. It should be noted that evanescent waves and inhomogeneous waves have the same mathematical representation, but in the interest of clarity, only the transmitted waves that result from supercritical incidence will be referred to as evanescent.

To illustrate the potential impact of inhomogeneous waves, consider a 2 m long interface of air and sea water, which have densities of $\rho_1 = 1.21$ kg/m^3 and $\rho_2 = 1026$ kg/m^3 and wave speeds of $v_1 = 343$ m/s and $v_2 = 1500$ m/s, respectively. Because of the large ratio of wave speeds, the critical angle is $\theta_c = 13.22°$. A 2 kHz plane wave incident at an angle of $\theta = 10°$ both reflects and transmits as a plane wave across the $z = 0$ boundary, as seen in Fig. 1.4. Note that although the maximum pressure amplitude is the same in both media, the amount of energy transmitted into the second medium is still extremely low because the impedance of water is much higher than that of air. If the same homogeneous plane wave is incident on the interface at

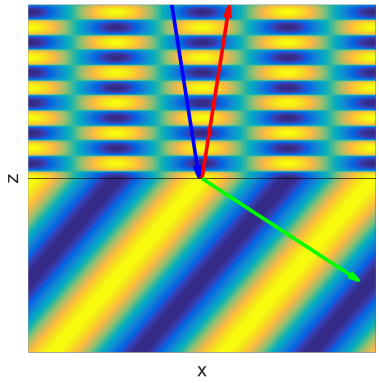

Figure 1.4. A diagram showing the interaction of a homogeneous plane wave incident (blue arrow) and reflected (red arrow) on a fluid–fluid boundary below the critical angle. A plane wave propagates into the second medium (green arrow).

$\theta = 15°$, slightly higher than θ_c, evanescent waves are created that propagate along the interface and decay into the medium. However, they do not propagate into the medium or dissipate energy, as seen in Fig. 1.5.

By introducing an inhomogeneity in the amplitude of the incident wave, as shown in Fig. 1.6, it can be seen that the waves created in the second medium appear

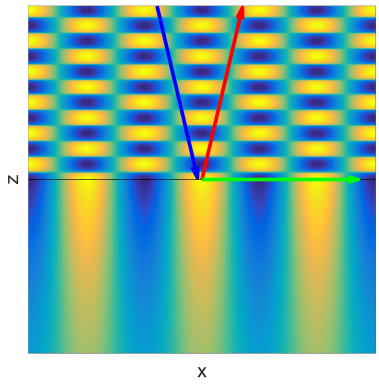

Figure 1.5. A diagram showing the interaction of a homogeneous plane wave incident (blue arrow) and reflected (red arrow) on a fluid–fluid boundary above the critical angle. Note the evanescent waves clinging to the interface in the bottom medium (green arrow).

evanescent but ultimately propagate away from the surface. This allows for the transfer of energy from one medium to another at an angle greater than θ_c.

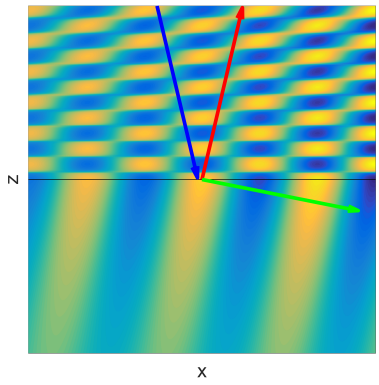

Figure 1.6. A diagram showing the interaction of an inhomogeneous plane wave incident (blue arrow) and reflected (red arrow) on a fluid–fluid boundary above the critical angle. Note the evanescent waves propagating into the bottom medium (green arrow).

With these parameters, the reflection coefficient is still close to but not equal to unity. However, at a near grazing angle and a small decay parameter of $\beta = 0.042$ rad/m, the reflection coefficient goes to zero and all incident energy is transmitted, as shown in Fig. 1.7.

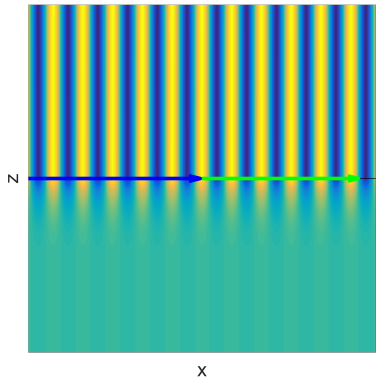

Figure 1.7. A diagram showing the interaction of an inhomogeneous plane wave incident (blue arrow) and reflected (red arrow) on a fluid–fluid boundary at a grazing angle. The evanescent waves propagating into the bottom medium (green arrow) carry all of the energy of the incident wave.

In order to exploit the Rayleigh phenomenon in solids, the optimal angle and decay parameter value must be determined. Of particular interest is the material Sylgard 184, which is used as a binder material for many energetic and mock energetic materials. Sylgard 184 has a density of $\rho = 1030$ kg/m^3, a longitudinal wave speed of $v_L = 1100$ m/s, and a shear wave speed of $v_S = 570$ m/s [15]. For a 2000 Hz plane wave in air incident on Sylgard 184, the Rayleigh angle is 40.32° and the corresponding decay parameter that allows for zero reflection is $\beta = 0.0043$ rad/m, as shown in Fig. 1.8. The optimum decay parameter scales directly with frequency, so a wave with double the frequency will require a decay parameter that is twice as large.

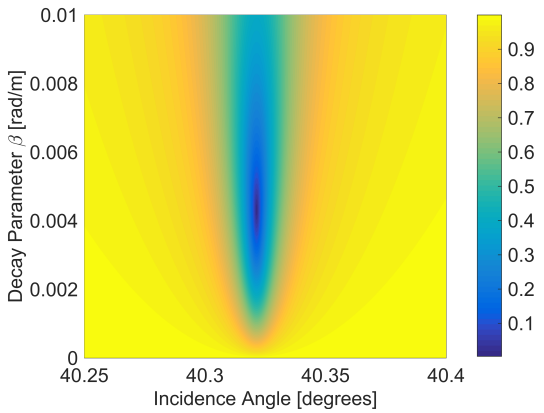

Figure 1.8. A diagram showing the minimization of the pressure reflection coefficient of a 2000 Hz inhomogeneous plane wave incident on Sylgard 184.

Inhomogeneous plane wave profiles of the form given in Eq. (1.17) are considered in the sound field reconstruction methods investigated in this work. In particular, broad ranges of the inhomogeneity parameter β are explored, in order to target efficient energy transmission [12, 13] into a wide range of solid materials.

In the context of acoustic energy transmission into solid media, at a particular frequency, the incidence angle θ and inhomogeneity parameter β are considered to be tunable in order to maximize the transmission. In Fig. 1.3, the fluid–solid interface is located at the $z = 0$ plane (with the fluid occupying the region $z < 0$ and the solid occupying the region $z > 0$), and Eq. (1.17) then represents the incident wave alone, and not the reflected wave (in the fluid) or the transmitted waves (in the solid) [10, 14].

It is well-known that the plane wave reflection coefficient is minimized, and the intensity transmission is maximized, with incidence near the Rayleigh angle, at which the incident wave efficiently excites the free wave solution along the solid surface [16–18]. Moreover, previous work has shown that, for lossless and low-loss fluid–solid interfaces, the inhomogeneity β can also be tuned to further reduce the reflection coefficient magnitude, and thus further increase the fraction of the incident energy which

is transmitted into the solid medium [12, 13]. It should also be noted that similar results have been shown for bounded incident waves, where the effective beamwidth may be tuned as well [19, 20].

As it is extremely difficult for a single simple source to create an inhomogeneous plane wave, other wave generation methods must be utilized, the easiest of which is an acoustic array with independent tunable sources. Though it is straightforward to adjust the incidence angle of an impinging wave on a solid surface with an acoustic array, adjusting the inhomogeneity of the incident wave requires additional consideration in the array design, particularly if large ranges of the inhomogeneity are considered. Specifically, for a set number of sources, the inhomogeneity affects the optimal source spacing, as quantified by the pressure errors and power consumption in the least-squares method. Here, the objective is to identify source array parameters that allow for the reasonable reconstruction of inhomogeneous plane waves over broad ranges of the incident wave inhomogeneity, β, which may be required for maximum energy transmission if solids with wide ranges of material properties are targeted.

2. RECONSTRUCTION OF ACOUSTIC PLANE WAVES

Portions of this chapter have been adapted from Kyle et al.: "Least-squares reconstruction of low-frequency inhomogeneous plane waves" [1].

2.1 Introduction

As was discussed in Chapter 1, it is generally infeasible to create inhomogeneous plane waves from a single source. Although the amplitude of a wave attenuates as an exponential function of distance to the source in a lossy medium, this attenuation is in the direction of propagation, not perpendicular to it as is required for an inhomogeneous wave.

Several factors must be weighed when evaluating the efficacy of a reconstruction method, the most important of which are error in pressure and power demand. The reconstructed wave profile must closely match the desired profile or the wave may not be correctly tailored to transmit into a desired material. If the reconstruction attempt requires a significant amount of power, it may not be electrically or mechanically feasible to drive the sources in the optimal manner.

Methods for the reproduction of arbitrary sound fields, including plane waves and random pressure fields, have been described in detail in a wide variety of contexts [21–28]. Commonly employed techniques include the least-squares method [23], the wave field synthesis approach [24], and the spectral division method [25, 27]. In the least-squares method, the desired pressure field is specified at a discrete number of points (e.g., on a receiver plane) and the least-squares algorithm is utilized to compute the source strengths (amplitudes and phases) for a specified number of sources and source locations [23]. Inevitably, a finite number of sources are used, and the generated pressure field is in error relative to the desired field, with that error depending on the

nature of the desired field, the separation distance, and the parameters which characterize the source and receiver arrays [23]. Moreover, errors in the regions between the receivers also occur (for a continuous desired pressure distribution), since a finite number of receivers are used in the solution algorithm.

In the context of inhomogeneous plane waves, which are investigated here as profiles which may enhance energy transmission into solid materials, approximations to such plane wave fields have, in fact, been previously generated [26, 29–32], and the reflection phenomena at solid interfaces have been documented in relation to plane wave theory [31]. However, no previous work has reported tuning the inhomogeneity in order to enhance energy transmission. It is thus the purpose of this work to apply the least-squares method for sound field reconstruction, using one-dimensional linear source and receiver arrays, to reproduce inhomogeneous plane wave fields over a range of inhomogeneity values. In particular, the source spacing will be varied to find values which simultaneously yield low errors in the generated pressure and low power consumption requirements over orders of magnitude of the incident wave inhomogeneity, which will make the array robust for a large range of incident wave parameters. A simple monopole point source model is considered, and the effects of the separation distance between the source and receiver locations are also addressed. Moreover, Gaussian noise distributions superimposed on the source amplitudes and phases will be introduced as a consideration for practical implementations, and the effects on the generated pressure field will be additionally explored.

2.2 The Least-Squares Method

The details of the least-squares method will be briefly outlined here, following the work of Kirkeby and Nelson [23]. Broadly speaking (and for any sound field reproduction method), in order to reconstruct a desired pressure field at a given standoff distance, the amplitudes and relative phases of the specified sources must be tuned to the appropriate levels. Note that unlike the methods of Itou et al. [26] and

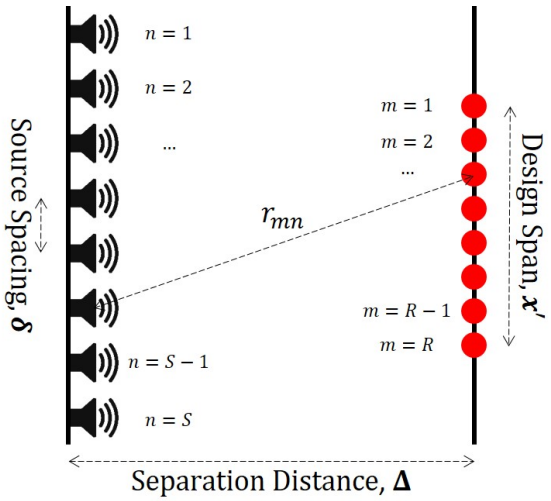

Figure 2.1. A diagram showing the one-dimensional linear source and receiver arrays.

Trivett et al. [29], which create true evanescent waves decaying away from the array, the least squares method creates a sound field that simply resembles evanescent waves decaying parallel to the array, and only on the plane specified by the standoff distance. In a one-dimensional linear array setup with S sound sources, the source strengths can be written as the elements of a vector $\tilde{\mathbf{Q}}$, with S elements. For a desired sound pressure distribution, $\tilde{p}(x)$, on a corresponding target surface, here taken to be a line, a finite number of points R must be chosen at which to evaluate (i.e., specify) the pressure or, in an experimental sense, to place the receivers. This sampled pressure distribution is then a vector $\tilde{\mathbf{P}}$ with R elements. A diagram showing the source-receiver array setup is given in Fig. 2.1, where x' is the coordinate on the design line. While the least-squares method can be used for any arbitrary distribution and alignment of sources and target receivers, the experimental setup discussed here will assume that the source line and the design line are parallel.

Since the generated pressure at any point in $\tilde{\mathbf{P}}$ is the sum of the sound pressures generated by each source in the source array, traveling varying distances and at vary-

ing angles, it is possible to relate the desired pressures $\tilde{\mathbf{P}}$ to the source strengths $\tilde{\mathbf{Q}}$ through the use of an impedance matrix $\tilde{\mathbf{Z}}$ [23]:

$$\tilde{\mathbf{P}} = \tilde{\mathbf{Z}}\tilde{\mathbf{Q}}, \tag{2.1}$$

or, with the elements expanded:

$$\begin{bmatrix} \tilde{P}_1 \\ \vdots \\ \tilde{P}_R \end{bmatrix} = \begin{bmatrix} \tilde{Z}_{11} & \cdots & \tilde{Z}_{1S} \\ \vdots & \ddots & \vdots \\ \tilde{Z}_{R1} & \cdots & \tilde{Z}_{RS} \end{bmatrix} \begin{bmatrix} \tilde{Q}_1 \\ \vdots \\ \tilde{Q}_S \end{bmatrix}. \tag{2.2}$$

With a monopole point source model employed for each of the sources, each element $\tilde{Z}_{mn}$ of the impedance matrix can be calculated as [23]:

$$\tilde{Z}_{mn} = \mathrm{i}\omega\rho\frac{\mathrm{e}^{-\mathrm{i}kr_{mn}}}{4\pi r_{mn}}, \tag{2.3}$$

where ρ is the density of the fluid medium and r_{mn} is the distance between receiver m at position $\mathbf{r_m}$ and source n at position $\mathbf{r_n}$, i.e.,

$$r_{mn} = |\mathbf{r_m} - \mathbf{r_n}|. \tag{2.4}$$

To remove the frequency dependence, Eq. (2.1) can be rewritten to give

$$\tilde{\mathbf{P}} = \tilde{\mathbf{H}}\tilde{\mathbf{a}}, \tag{2.5}$$

where $\tilde{\mathbf{H}}$ is the modified impedance matrix and $\tilde{\mathbf{a}}$ is the vector of source volumetric accelerations. Thus, with the relationships [23]:

$$\begin{aligned} \tilde{\mathbf{H}} &= \frac{1}{\mathrm{i}\omega}\tilde{\mathbf{Z}}, \\ \tilde{\mathbf{a}} &= \mathrm{i}\omega\tilde{\mathbf{Q}}, \end{aligned} \tag{2.6}$$

the accelerations, and therefore the source strengths, can be determined by solving the matrix equation.

Since it is not required that R equals S, Eq. (2.5) does not, in general, have a unique, exact solution. Thus, as in the case of an overdetermined system, an approximate method for the solution is necessary. For the least-squares fitting model,

the components of the source acceleration vector $\tilde{\mathbf{a}}$ are determined through the equation [23]:

$$\tilde{\mathbf{a}} = \left(\tilde{\mathbf{H}}^{*}\tilde{\mathbf{H}}\right)^{-1}\tilde{\mathbf{H}}^{*}\tilde{\mathbf{P}}, \tag{2.7}$$

where $\tilde{\mathbf{H}}^{*}$ denotes the complex conjugate transpose of the modified impedance matrix. The actual pressure distribution at the target can be evaluated by multiplying the modified impedance matrix by the acceleration vector given in Eq. (2.7).

The complex source strengths can be found by applying Eq. (2.6), and the monopole source input powers can then be found through the equation [33]:

$$W_n = \frac{|\tilde{Q}_n|^2 \rho v k^2}{8\pi}. \tag{2.8}$$

The total acoustic power required for the array can be found by summing the monopole powers. This assumes that the source powers are not correlated, and although this sum will not be exactly equal to the true electrical power demand of the entire array, it is useful as a metric of how much electrical power will be required to drive the sources. While not particularly meaningful in a theoretical sense, this piece of information is important to note when considering the practicality of real experimental applications of the array. Note that the relative phase offset of each source is determined as the phase of the complex source strength:

$$\phi_n = \arctan \quad \frac{\mathrm{Im}[\tilde{Q}_n]}{\mathrm{Re}[\tilde{Q}_n]}\Bigg)\Bigg(\tag{2.9}$$

It should be further emphasized here that the pressure field from each source is harmonic in time, through the dependence $\mathrm{e}^{\mathrm{i}\omega t}$, and that the relative phases, ϕ_n, among the sources serve to reproduce the desired pressure field at the receivers through the interference of the respective generated fields.

2.3 Theoretical Results

To evaluate the performance of an acoustic array, a consistent basis will be used in the course of this analysis: 8 sound sources with a frequency of 10 kHz; 8 design

points over the span of 17.5 cm; and room temperature air as the medium. While many of these parameters are able to be modified, only certain general cases will be explored in depth.

By using the least-squares reconstruction method, it is possible to determine the pressure error profile on the target surface and the source power profile. The optimum experimental setup occurs when both the pressure errors and source powers are minimized, as an inaccurate pressure profile will be ineffective at energy transmission and a high value for source power will be difficult to physically achieve and sustain.

In the case of homogeneous plane waves, the vector $\tilde{\mathbf{P}}$ will have elements that are all equal in value, while in the case of inhomogeneous plane waves, the values of the elements will be determined by evaluating an exponential function at the target points. To provide a comparison of wave types, homogeneous plane wave examples will be shown first, followed by a detailed analysis of inhomogeneous plane waves.

For a normally incident homogeneous plane wave with an amplitude of 1 Pa (the source array and target surface are aligned), every element of $\mathbf{P}$ is real and equal to unity. It is a simple matter to turn this reconstructed homogeneous plane wave into an inhomogeneous plane wave by adding an exponential decay parameter, β. Thus, instead of the desired pressure profile being a uniform 1 Pa, it now takes the form $\Gamma e^{\beta x'}$, with Γ determined such that the pressure at the edge of the design span equals 1 Pa, and x' representing the position along the design line. For this analysis, the decay parameter will take a relatively high value of $\beta = 1$ rad/m in order to provide an extreme limit in contrast to the homogeneous wave. By assuming that the sources are monopoles with an equal spacing of $\delta = 6$ cm and that the standoff distance between the sources and receivers is $\Delta = 50$ cm, the pressure profiles can be generated using Eq. (2.5), and are shown in Fig. 2.2. In this case, there are 8 design points, each separated by 25 mm. These design points are simply used as parameters in the least-squares algorithm, and do not necessarily correspond to physical microphones or receivers on the target surface.

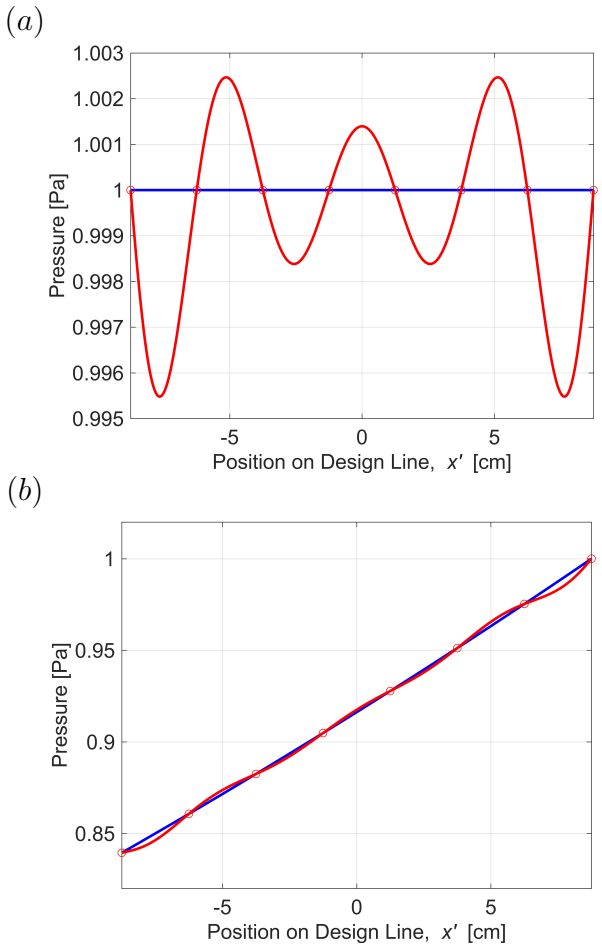

Figure 2.2. A diagram comparing the magnitude of the pressure distribution of a reconstructed (a) homogeneous plane wave and (b) inhomogeneous plane wave with decay parameter $\beta = 1$ rad/m. The ideal 1 Pa plane wave is shown in blue and the reconstructed wave is shown in red.

Noticeably, the error in pressure magnitude essentially vanishes at the 8 target points, but the errors can become significant between those points. By subtracting the ideal pressure distribution from the generated profile, the error can be plotted. As shown in Fig. 2.3, the maximum error along the design span for a homogeneous wave under the given conditions is 4.5×10^{-3} Pa, or 0.45%. In the case of the inhomogeneous wave, the error pattern is no longer completely symmetric, but scales slightly higher as the pressure gradient increases. This is indicative of the difficulty in fitting a pressure distribution that changes significantly over a small distance. The maximum error for an inhomogeneous wave is 4.6×10^{-3} Pa, or 0.47%.

The homogeneous plane wave requires a total acoustic power of 3.5 mW from the sources, distributed symmetrically as seen in Fig. 2.4a. This symmetry is lost for the case of the inhomogeneous plane wave (Fig. 2.4b), which, because it ultimately demands lower pressure magnitudes on the design surface, only requires 3.0 mW.

In this analysis, the span of the sound sources is 2.4 times wider than the target surface due to the physical experimental limitations of the sources themselves. As such, sources near the edges of the array do not significantly contribute to the overall consumption of power, even in the case of an inhomogeneous wave.

The distribution of initial source phases is also shown in Figs. 2.5a and 2.5b. While small deviations exist, the sources are almost in phase with each other. Even when the power symmetry is broken in the case of the inhomogeneous wave, the phase range does not significantly expand.

As was mentioned in the previous section, the number of sources and the number of design points are not required to be equal. By increasing the number of design points from 8 to 128 on the same target span, the root mean square error is reduced from 2.1×10^{-3} Pa to 1.6×10^{-3} Pa. The resulting pressure distribution, as seen in Fig. 2.6, is closer to the desired pressure distribution of 1 Pa. While this reduction in error is appreciable, experimentally, it is not currently possible to verify the pressure at so many locations over such a small range. Because of this limitation, the 8-point model will be used.

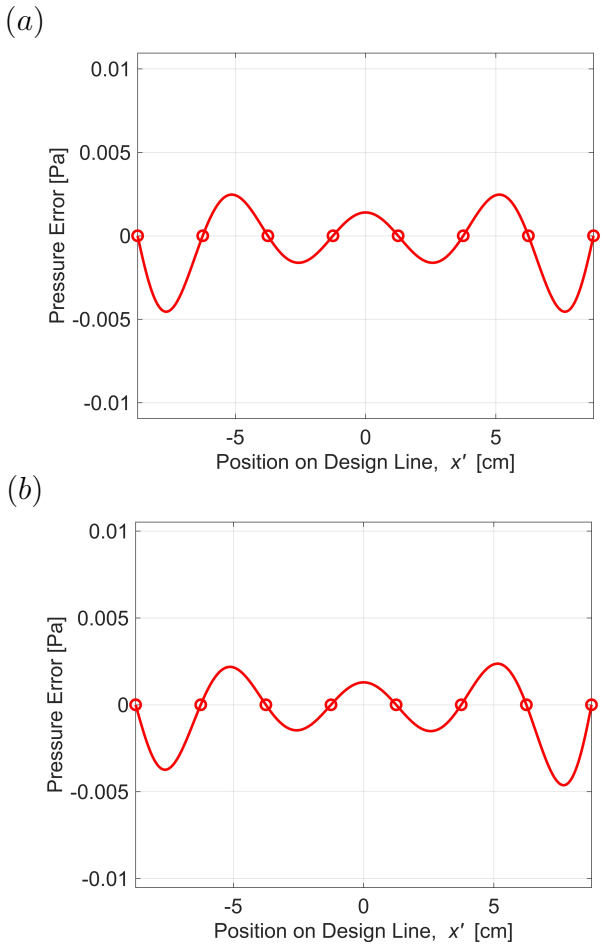

Figure 2.3. A diagram comparing the magnitude of the maximum pressure error of a reconstructed (a) homogeneous plane wave and (b) inhomogeneous plane wave with decay parameter $\beta = 1$ rad/m.

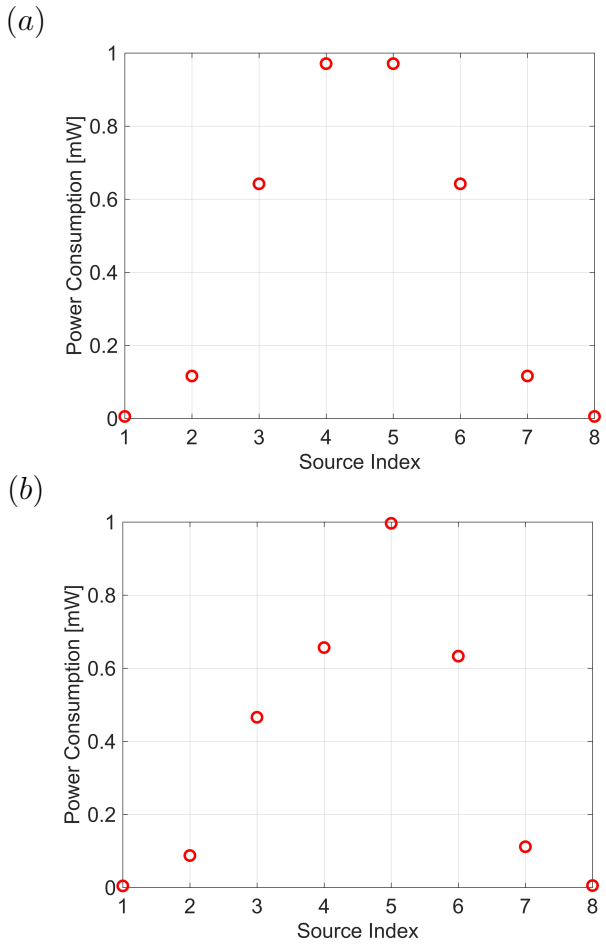

Figure 2.4. A diagram comparing the magnitude of the required acoustic source powers for (a) a homogeneous plane wave and (b) an inhomogeneous plane wave with decay parameter $\beta = 1$ rad/m.

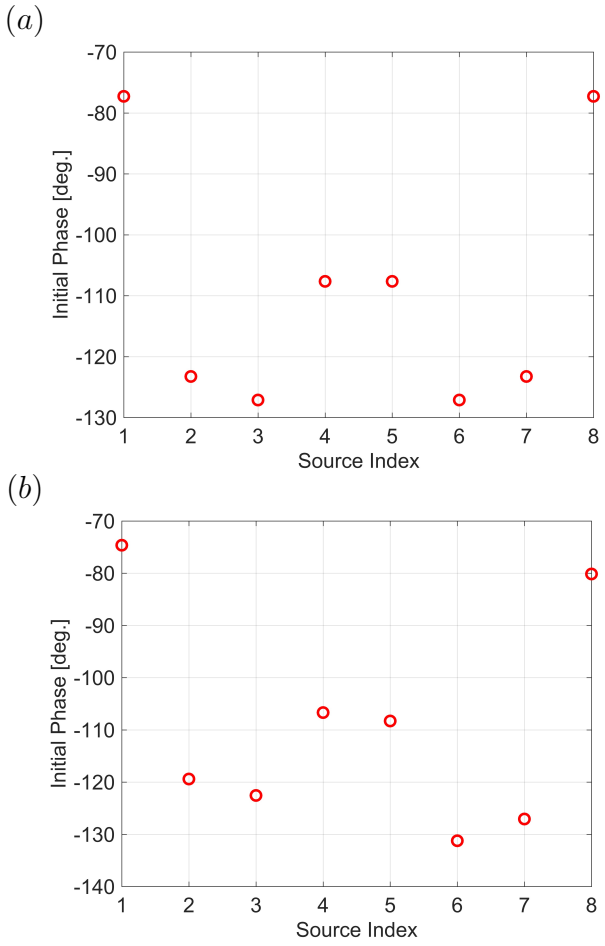

Figure 2.5. A diagram comparing the initial source phases for (a) a homogeneous plane wave and (b) an inhomogeneous plane wave with decay parameter $\beta = 1$ rad/m.

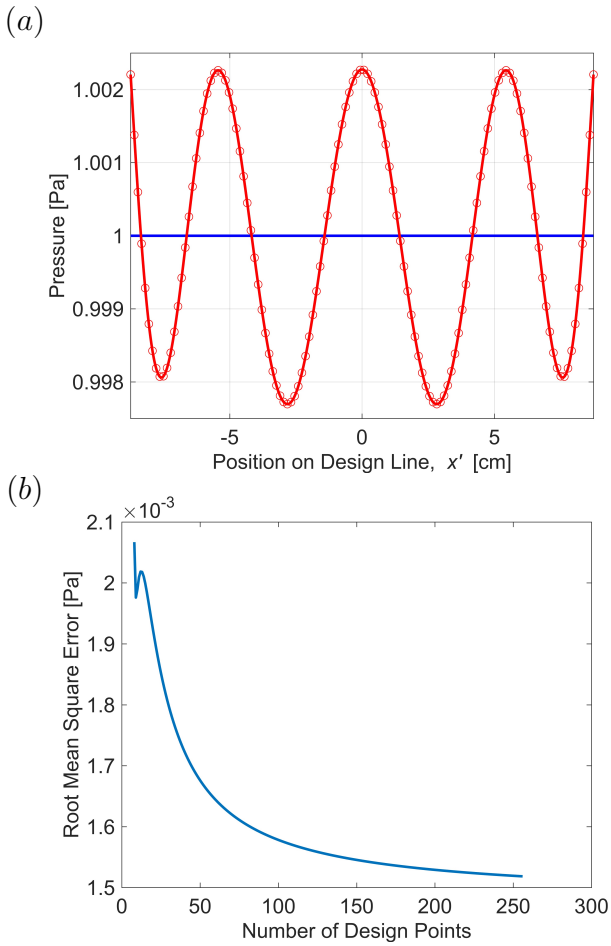

Figure 2.6. (a) A diagram showing the reproduced homogeneous pressure distribution when 128 design points are used, and (b) the root mean square error of a homogeneous wave as a function of the number of design points.

2.3.1 Variation of Array Parameters

The possibility of a large standoff distance between the array and the target surface is critically important to real world applications of this apparatus, as in some cases, it may be difficult or dangerous to deploy an array very close to a target material. As seen in Fig. 2.7, the maximum error in pressure decreases with increasing standoff because the spherical waves begin to naturally appear more like plane waves. However, if a very large standoff is attempted, a significant amount of power could be required due to the spatially decaying nature of spherical waves. Despite the power demand growing exponentially with respect to standoff distance, as seen in Fig. 2.8, both homogeneous and inhomogeneous waves can be generated with relatively low power outputs from the sources for the current parameters of interest.

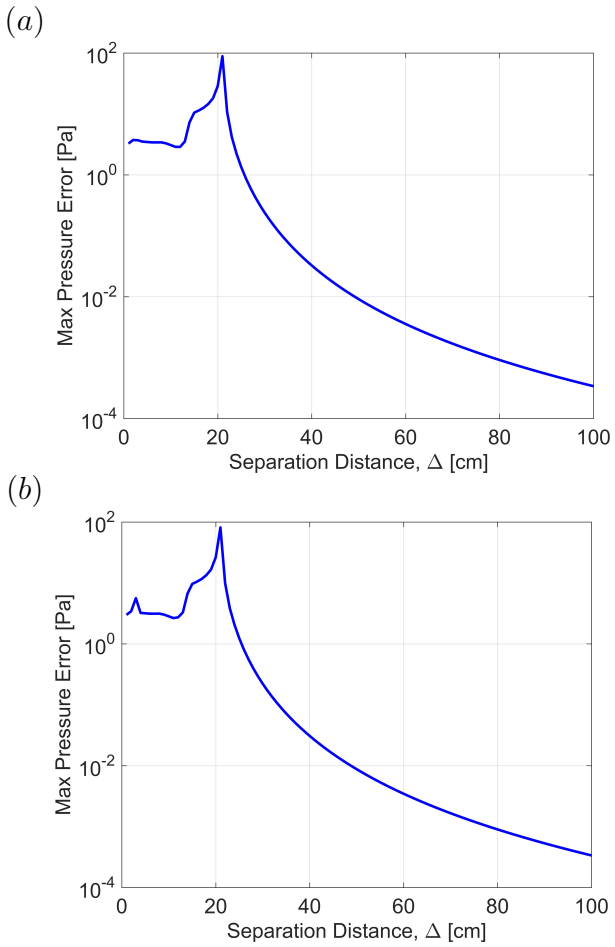

Figure 2.7. A diagram comparing the maximum pressure error with respect to varying separation distance for (a) a homogeneous plane wave and (b) an inhomogeneous plane wave with decay parameter $\beta = 1$ rad/m.

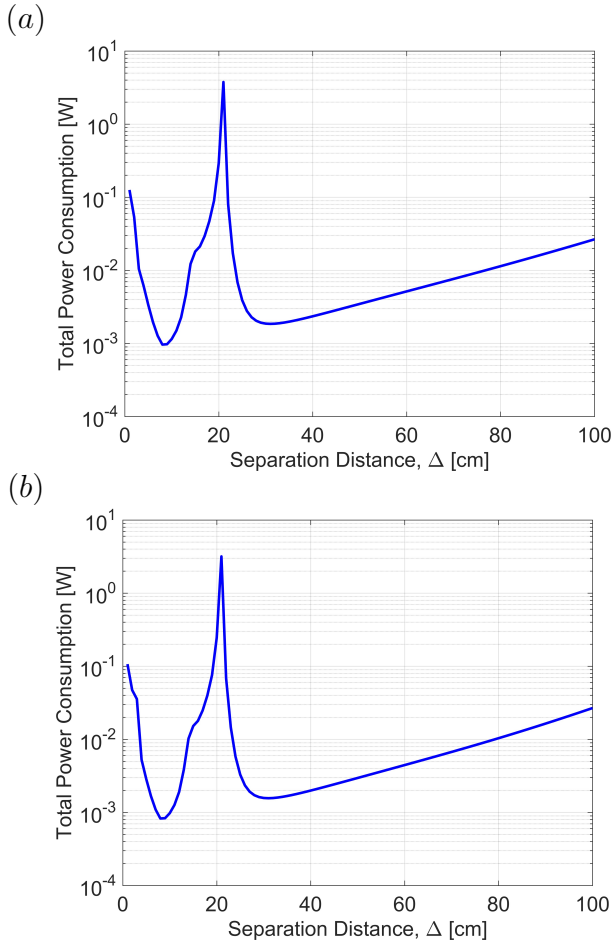

Figure 2.8. A diagram comparing the total acoustic power consumption with respect to varying separation distance for (a) a homogeneous plane wave and (b) an inhomogeneous plane wave with decay parameter $\beta = 1$ rad/m.

A large spike in errors and power consumption occurs at approximately $\Delta = 20$ cm for this configuration, as the source spacing and standoff distance were such that in order to match the desired pressure distribution at the design points, a significant amount of power was required. While errors at the design points were still small, errors in the spaces between them were large due to the excessive power of the sources and the near-singular nature of the impedance matrix as specified in Eq. (2.1). Kirkeby and Nelson noted this issue, specifying that the matrix to be inverted is poorly conditioned [23]. This is not only an issue with numerical solvers, but also indicative that

very small errors in the source accelerations, even rounding errors, could cause a drastically different pressure distribution from the one desired [23]. A smoother curve in Figs. 2.7 and 2.8 can generally be obtained by increasing the number of design points, or by increasing both the number of design points and the number of sources. While numerical methods exist to compensate for poor conditioning, it is generally recommended to avoid specifying design parameters that cause near-singular matrices due to the relatively high level of error that will result during reconstruction. Because of this restriction and prohibitively high pressure error, the only practical separation distances are those greater than 20 cm, for this case.

The minimum value of total power consumption for an inhomogeneous wave occurs at a standoff distance of $\Delta = 31$ cm (barring the highly erroneous case when the standoff distance is 10 cm). While the power is very low at 1.6 mW, the corresponding maximum pressure error is 19.2%. Thus, in the scope of practical applications, it will be important to quantify whether reducing the pressure error or reducing the power consumption is the dominant design criterion.

Fig. 2.9 illustrates the effect of varying both source spacing and standoff distance, with the color bar representing the logarithm of maximum pressure error in pascals. It can be seen that in general, as source spacing increases, a greater standoff distance is required to maintain a low level of error. Of note is the dark red strip which represents an extreme error in pressure, which was previously seen in Fig. 2.7. While there are slight variations in pressure error between the homogeneous and inhomogeneous waves, it is not significant, and as a result, part (b) of the figure shows the logarithm of the difference of maximum errors between homogeneous and inhomogeneous waves.

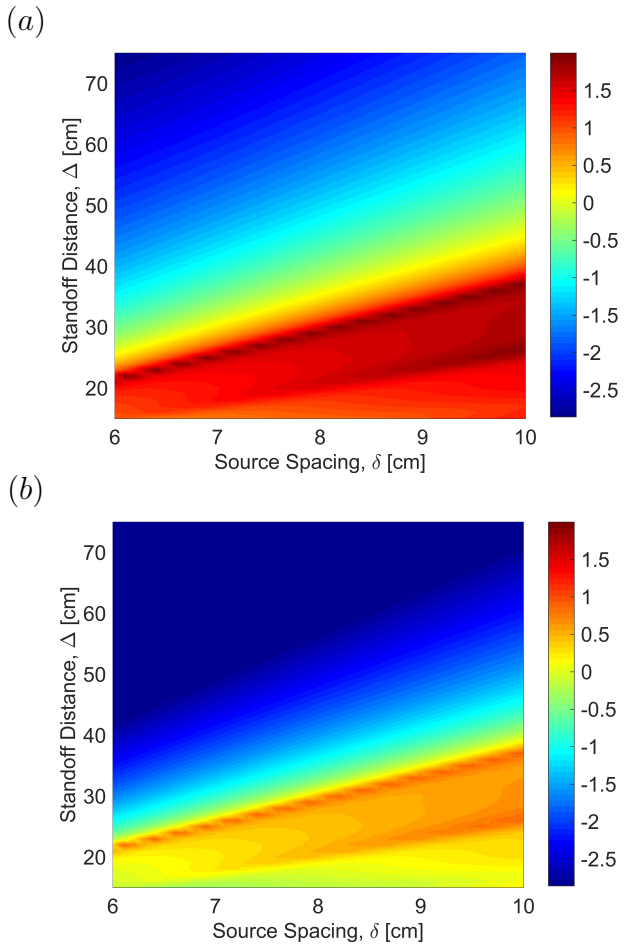

Figure 2.9. A diagram comparing (a) the logarithm of maximum pressure error (in Pa) with respect to varying separation distance and source spacing for a homogeneous plane wave and (b) the logarithm of the difference in maximum pressure error (in Pa) with respect to an inhomogeneous plane wave with decay parameter $\beta = 1$ rad/m.

Fig. 2.10 shows how source spacing and standoff distance affect the total power consumption by the sources, with the color bar representing the logarithm of total acoustic power in watts. The strip of highest power corresponds to the strip of highest pressure error as seen in the previous figure, and in general, no waveform reconstruction should be attempted in the region below this strip due to these high values of power consumption and pressure error. For a given source spacing, there is an optimal standoff distance that will require the least amount of power. Increasing

the standoff reduces pressure errors, but it increases power consumption. Again, the results for the homogeneous case and the inhomogeneous case are very similar, so Fig. 2.10b shows the logarithm of the difference in total acoustic power between the homogeneous and inhomogeneous waves.

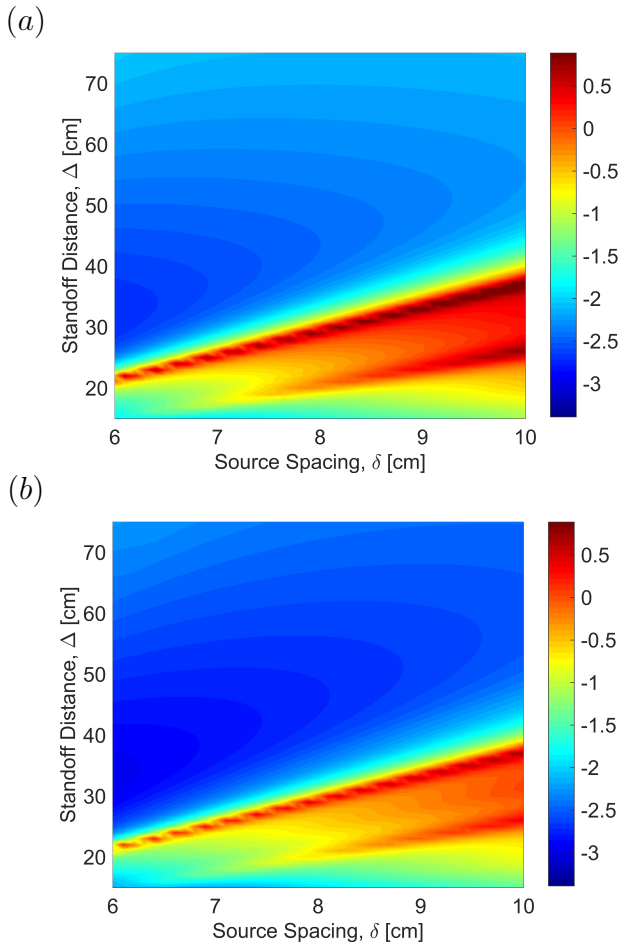

Figure 2.10. A diagram comparing (a) the logarithm of total acoustic power consumption (in W) with respect to varying separation distance and source spacing for a homogeneous plane wave and (b) the logarithm of the difference in total acoustic power (in W) with respect to an inhomogeneous plane wave with decay parameter $\beta = 1$ rad/m.

As the range of parameters shown only encompasses a small portion of the possible standoff distance and source spacing values, it is possible to broaden the scope of the

simulation to investigate notable mathematical artifacts. Fig. 2.11a shows the maximum pressure error and Fig. 2.11b shows the power consumption of a homogeneous plane wave, with the source spacing varying up to 20 cm and the standoff distance varying up to 10 m.

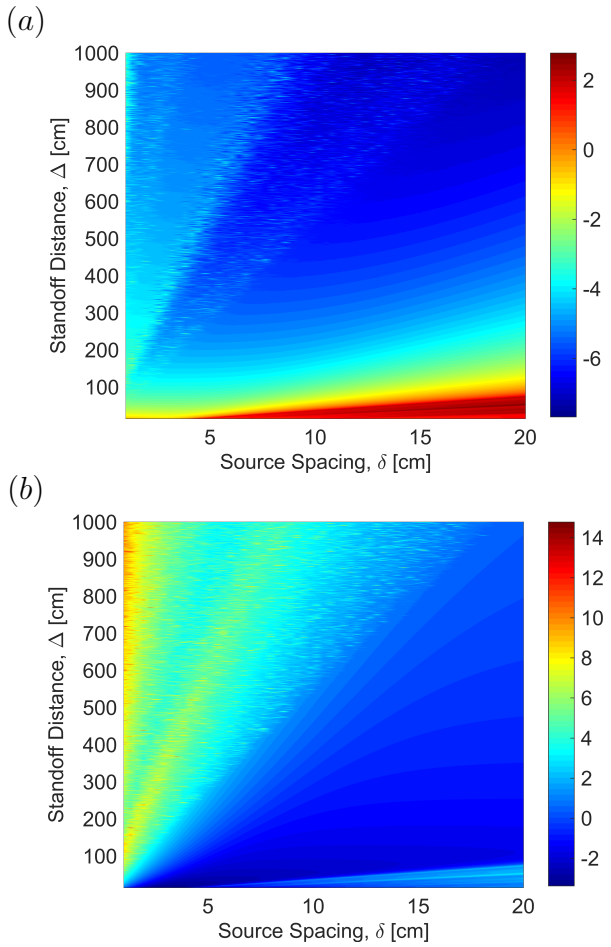

Figure 2.11. A diagram comparing (a) the logarithm of maximum pressure error (in Pa) and (b) the logarithm of total acoustic power consumption (in W) with respect to significantly varying separation distance and source spacing for a homogeneous plane wave.

It can be seen that at large standoff distances, pressure errors remain generally low, but there are discontinuities in the plot. The region where this occurs is more readily apparent in Fig. 2.11b, where the power requirement is unreasonably high.

This region, like the small-standoff region, is a result of a near-singular impedance matrix. Since each row of the impedance matrix corresponds to the distance between a given design point and every source, at very large standoff distances, the spacing of the sources and the length of the design line become negligible. This is especially true for the design points in the middle of the design line, and as a result, the innermost rows of the impedance matrix are extremely similar, resulting in a poorly conditioned matrix. At this distance, the waves from the individual sources are already nearly planar, making some of them redundant. Thus, a valid method to reduce the power demand at large standoff distances is to make the system overdetermined by reducing the number of sources.

After choosing a 50 cm standoff distance and introducing inhomogeneity, it is revealed that errors in pressure, and the maximum power consumption, are largely controlled by the source spacing, with little dependence on the degree of inhomogeneity. This is not surprising, as Figs. 2.9b and 2.10b show very small differences. Figs. 2.12 and 2.13 show plots of pressure error and power consumption as a function of source spacing and decay parameter, with the color bars representing those quantities in pascals and watts.

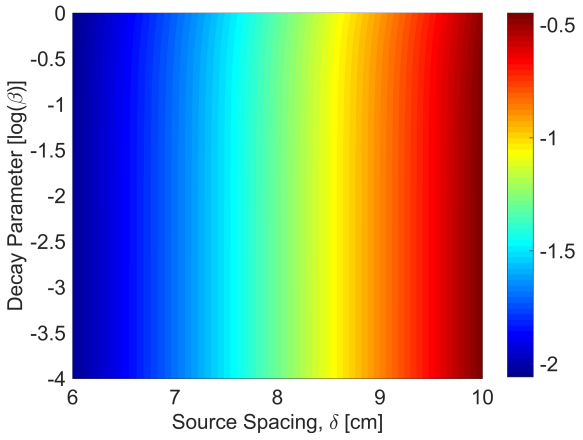

Figure 2.12. A diagram showing the logarithm of maximum pressure error (in Pa) with respect to varying decay parameter and source spacing for an inhomogeneous plane wave at a standoff distance of 50 cm.

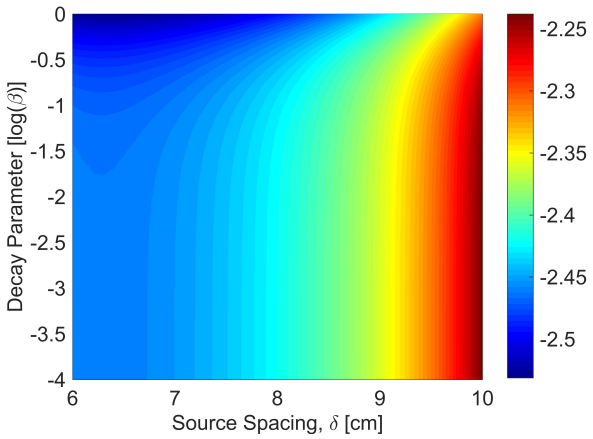

Figure 2.13. A diagram showing the logarithm of total acoustic power consumption (in W) with respect to varying decay parameter and source spacing for an inhomogeneous plane wave at a standoff distance of 50 cm.

The total power consumption appears to be loosely correlated with the decay parameter, but only when it reaches relatively high values on the order of $\beta = 1$ rad/m. As the degree of inhomogeneity required for many transmission applications is several orders of magnitude less than this, it does not appear as though introducing a degree of inhomogeneity to a wave field will adversely affect either the accuracy of the reconstructed wave or the source powers required to generate the wave.

2.3.2 Sensitivity of Reconstruction to Source Inconsistencies

In a realistic experimental setup, each source will not be exactly tuned to the specified power and phase necessary for the least-squares solution. By first identifying the least-squares solution and then simulating the results when small Gaussian-distributed errors are applied to each source, an error band can be generated to show an expected range of values for the magnitude of the reconstructed plane wave.

To investigate the effects of adding Gaussian errors to both source power and initial phase offset, 5000 simulations were first run with only errors in phase and then with only errors in power. Fig. 2.14 shows the average magnitude for both a

reconstructed homogeneous plane wave and an inhomogeneous plane wave, assuming a Gaussian error in initial source phase with a mean value of 0 degrees and a standard deviation of 1 degree, a value intended to capture small perturbations but still remain physically plausible. At any given point on the target surface, the expected maximum deviation from the target pressure distribution is 2.1% for the homogeneous case and 2.3% for the inhomogeneous case.

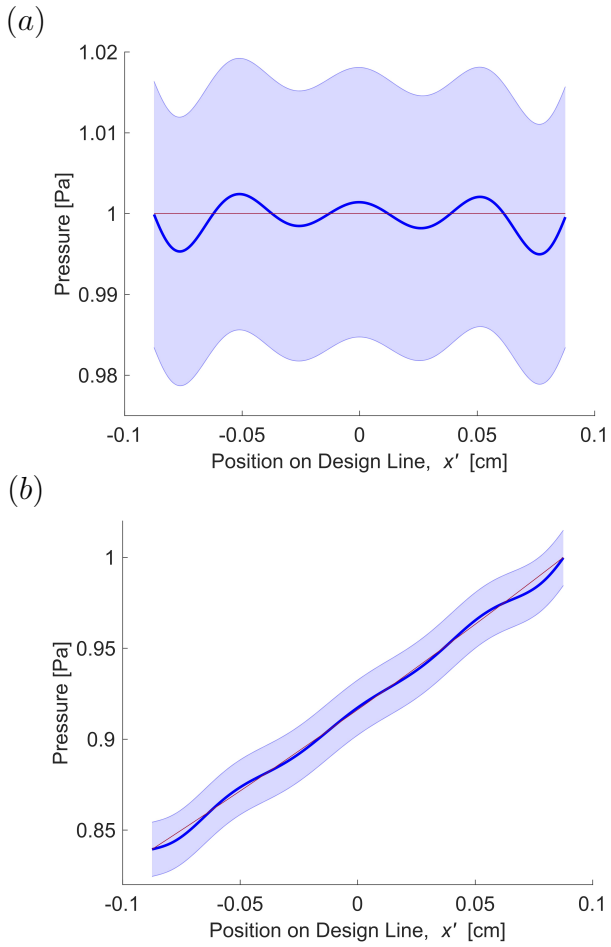

Figure 2.14. A diagram comparing the effects of adding a Gaussian error in initial source phase (mean value of 0 degrees and standard deviation of 1 degree) on the average magnitude of the pressure distribution (bounded by one standard deviation) of a reconstructed (a) homogeneous plane wave and (b) inhomogeneous plane wave with decay parameter $\beta = 1$ rad/m.

Fig. 2.15 show the results of the same simulation, but with a zero-mean, 1% standard deviation Gaussian error in source power and no error in phase angle. This standard deviation, again, is meant to represent a relatively small but still realistic source error. The maximum error in pressure is about 0.92% for the homogeneous case and 0.94% for the inhomogeneous case, much less than the variation caused by the phase error that was explored.

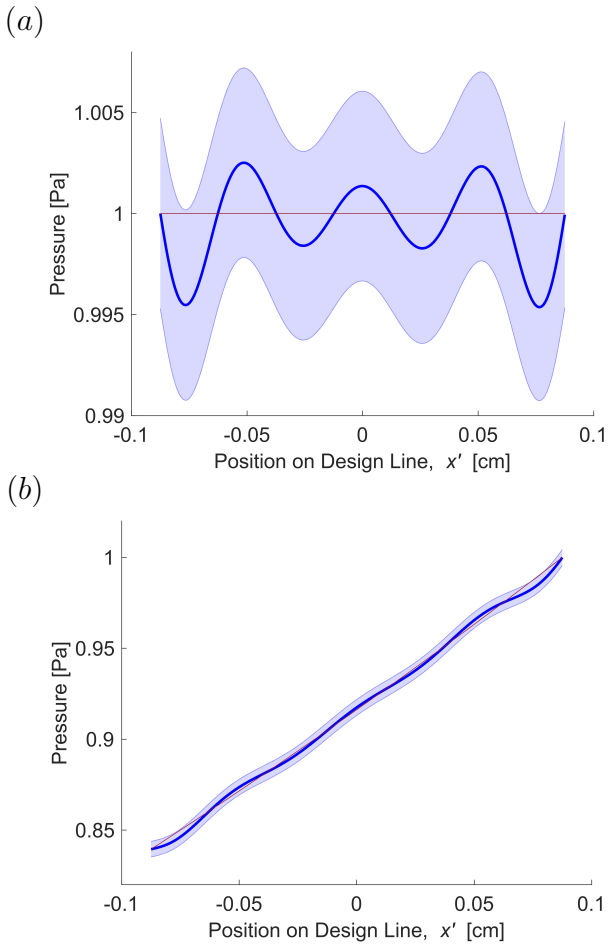

Figure 2.15. A diagram comparing the effects of adding a 1% Gaussian error in source power on the average magnitude of the pressure distribution (bounded by one standard deviation) of a reconstructed (a) homogeneous plane wave and (b) inhomogeneous plane wave with decay parameter $\beta =$ 1 rad/m.

As, in this case, the error in phase angle dominates the error in source power, the combination of a 1 degree phase error and a 1% power error yields a maximum deviation of 2.2% from the desired pressure in a homogeneous wave and 2.3% in an inhomogeneous wave, as seen in Fig. 2.16.

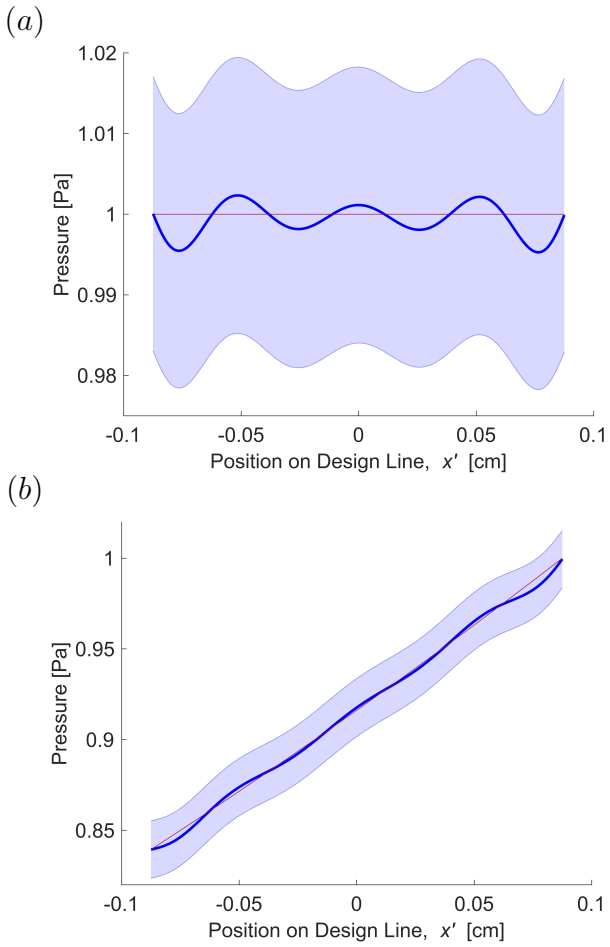

Figure 2.16. A diagram comparing the effects of adding both Gaussian error in initial source phase (mean value of 0 degrees and standard deviation of 1 degree) and a 1% Gaussian error in source power on the average magnitude of the pressure distribution (bounded by one standard deviation) of a reconstructed (a) homogeneous plane wave and (b) inhomogeneous plane wave with decay parameter $\beta = 1$ rad/m.

By fitting an exponential curve to the extreme values of the pressure standard deviation, bounds for the decay parameter can be determined. In this case, β has a

range of 0.804 rad/m to 1.198 rad/m. This variation can have a significant impact on the pressure reflection coefficient when the inhomogeneous wave is incident on a solid surface.

For example, for a wave incident on a solid material such that the density ratio $\rho_2/\rho_1 = 1000$, the longitudinal wave speed ratio $v_{2_L}/v_{1_L} = 10$, and the shear wave speed ratio $v_{2_S}/v_{1_L} = 7$, the optimal angle of incidence θ is 9.37 degrees, the optimal decay parameter β is 1.06×10^{-3} rad/m, and the resulting magnitude of the pressure reflection coefficient $|R|$ is 0 [12, 34]. If the aforementioned errors are present in the sources, β can vary from 0 rad/m to 0.1955 rad/m, and it can be clearly seen that $|R|$ increases substantially even with small changes to β (Fig. 2.17). Ultimately, even small errors in a sound source could hinder the ability to transmit energy into a material if the inhomogeneous wave is not properly formed.

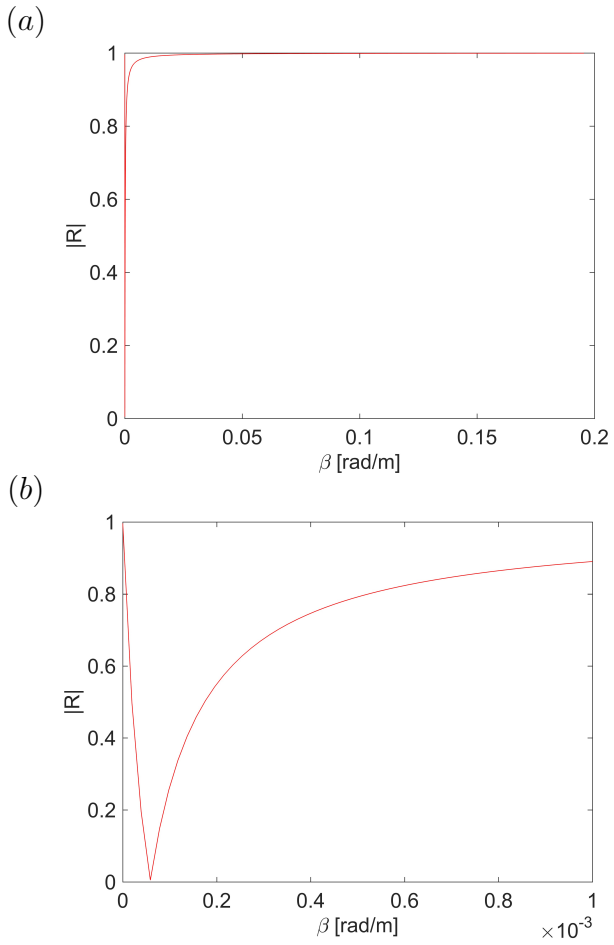

Figure 2.17. (a) A diagram showing the effects of varying the decay parameter β on the magnitude of the reflection coefficient $|R|$ when an inhomogeneous wave is incident on a solid material at the optimal angle, and (b) a zoomed-in view of the same diagram to highlight the results near $\beta = 0$ rad/m.

The actual process of signal generation requires numerous electrical components that could delay the signal, effectively changing the phase. Particularly at such a high frequency as 10 kHz, phase angle errors could prevent the accurate reconstruction of plane waves. If these errors are consistent and systemic, however, compensations can be added to the data acquisition system in order to remove them.

2.4 Conclusions

In order to reconstruct a spatially decaying plane wave at a specified target surface, the acoustic power outputs and relative phases of sound sources organized in a linear array can be tuned to cause pressure interference in the desired manner. By modeling a realistic source array using 8 sources, each separated by $\delta = 6$ cm, and a target microphone array with 8 design points, each separated by 25 mm, at a standoff of $\Delta = 50$ cm, an inhomogeneous plane wave can be reconstructed with minimal error and acoustic power consumption. While the sources do vary significantly in terms of power output, their respective phases are relatively similar.

Since the minimum ratio of source array span to target span is dictated by physical constraints to be 2.4 in this investigation, an increase of source separation increases both pressure errors and power consumption. An increase of standoff distance always reduces pressure errors and generally increases power consumption, but due to the fact that certain combinations of parameters lead to near-singular impedance matrices, there is an optimal standoff distance for any given source spacing that minimizes power consumption. However, by evaluating the pressure distribution at the parameters of minimum power, it is clear that the pressure errors that occur at those parameters are rather high, suggesting that many operating points for an acoustic array will not be at the optimized parameter for minimum power.

The addition of inhomogeneity to homogeneous plane waves did not significantly affect the maximum pressure error or total power consumption, leading to the optimistic assertion that inhomogeneous waves are not more difficult to physically reconstruct than homogeneous waves. Inhomogeneous waves follow the same trends as homogeneous waves, with total source power generally increasing with both source separation and standoff distance.

When errors are added to the sources in terms of power and phase deviations, the effects on any individual pressure distribution can be significant. However, the average magnitude of pressure across many simulations tends towards the least-squares

solution. Errors in relative phase angle can cause significant variation in generated pressure distributions, so any time lag in signal generation must be quantified in order to ensure that the appropriate phase relations are met.

This work is unique with respect to previous work in that it does not create true evanescent waves that decay away from the array; it reconstructs inhomogeneous plane waves that have a similar mathematical representation and similar expected physical properties to evanescent waves at a defined plane. This technique will be useful in expanding the capabilities of arrays transmitting energy into solid materials, a task which generally requires the use of spatially decaying waves.

3. PHYSICAL IMPLEMENTATION OF THE LEAST-SQUARES METHOD

3.1 Introduction

Based on the simulation presented in Chapter 2, an experimental setup comprising the source and receiver arrays was developed. The source array was constructed out of 80/20 T-slotted aluminum framing, and comprised of four crossbars, each with a length of 6 feet (1.83 m). The top bar of the array is 4 feet (1.22 m) above the ground and the other bars are spaced equidistantly with respect to each other, though their positions are adjustable.

The sources selected were Pyle PDBT35 1" Titanium Super Tweeters, with a power rating of 500 W peak, and an electrical impedance of 4-8 Ω. These sources were selected based on their compactness, cost, and pressure frequency response, which was reported to be highest in the range of 2-22 kHz. The 32 tweeters were distributed along the four crossbars of the array, although for most of the following tests, only the 8 sources on the top bar were used. This facilitated a less cumbersome evaluation of the least-squares algorithm, as the array was linear rather than planar. The sources were powered by Crown DCi 8/300N 8 Channel BLU Link Power Amplifiers, each of which could supply 300 W across 8 sources and apply a voltage gain of 34 dBV. The input voltage, phase, and frequency were controlled by a National Instruments PXIe-8840 Quad-Core Data Acquisition System (DAQ) through a LabVIEW Virtual Instrument, with the signals being sent through a PXIe-6739 16-bit Analog Output card coupled with two SCB-68A Connector Blocks. The source array setup can be seen in Fig. 3.1, and the DAQ can be seen in Fig. 3.2.

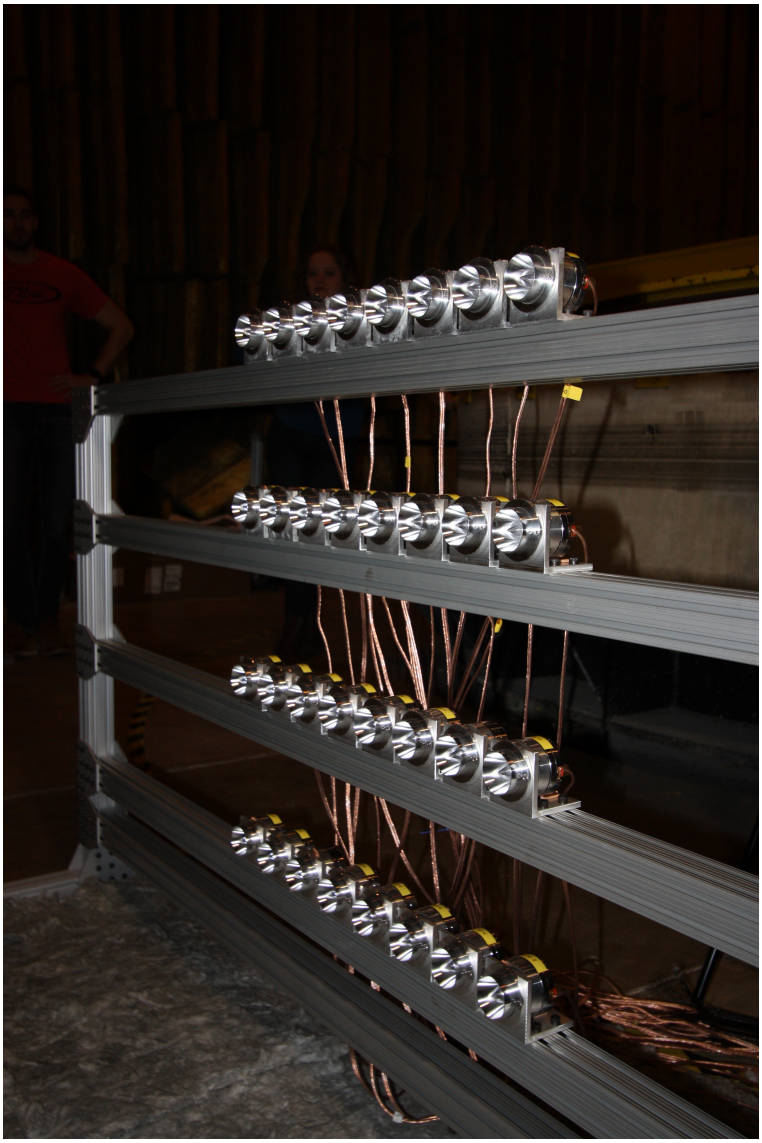

Figure 3.1. A diagram showing the source array, with the 32 tweeters evenly distributed among the crossbars.

Figure 3.2. A diagram showing the data acquisition systems for both the source array and receiver array.

The receiver array also comprised of four crossbars, each with a length of 6 feet (1.83 m). The heights of the crossbars were all easily adjustable, so the top bar was aligned to the same height as the top bar of the source array. Microphone clips with a thickness of 0.375 inches (0.95 cm) were attached to the bars at regular intervals that were dictated by the test parameters.

The microphones selected were PCB Piezotronics ICP Free-Field Array Microphones, Model 130F21. The frequency response of these microphones was reported to be within 4 dB over the range of 10-20,000 Hz. The 64 microphones were distributed along the four crossbars of the array, and were easily movable. Like the sources, only the microphones on the top bar were typically utilized due to the linear nature of the tests. Signals from the microphones were processed by several National Instruments PXIe-4497 24-Bit Sigma-Delta Analog-to-Digital Converters, and the digital signals were interpreted by a separate but identical DAQ through a LabVIEW Virtual Instrument. The receiver array setup can be seen in Fig. 3.3.

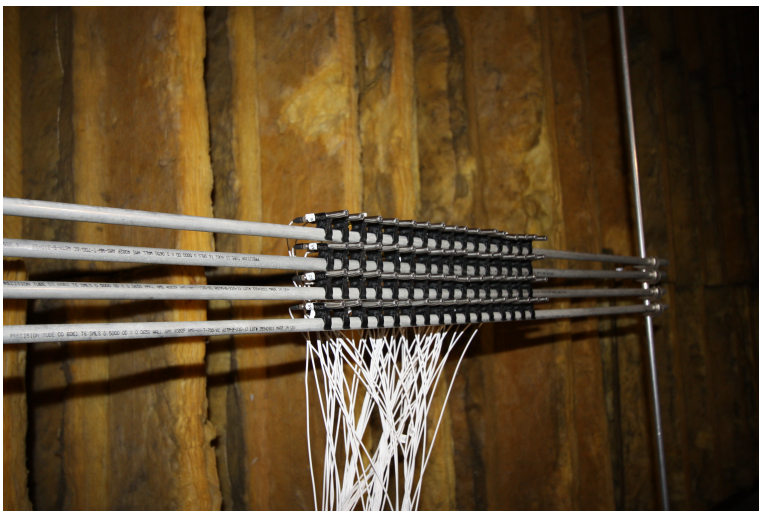

Figure 3.3. A diagram showing the array of microphones, with the 64 receivers distributed among the crossbars.

The microphones were calibrated using a PCB Piezotronics CAL250 pistonphone outputting 114 dB at 251.2 Hz. Supplied with the microphones were calibration sheets with each frequency response plotted over the operating range, with respect to 250 Hz. These frequency responses were sampled and used to adjust the reported pressure magnitudes to their true values over the range of 2-15 kHz. The tests were

performed in both a fully anechoic chamber and a hemi-anechoic chamber with absorptive material on the floor.

3.2 Source Characterization

A key assumption of the least-squares algorithm is that each source is a perfect monopole, with the pressure field at any given distance not depending on a radial angle. Pressure decays with the inverse of distance, and sound power decreases with the inverse of the distance squared. In real sources, however, small deviations from these ideal behaviors exist, even at low frequencies. Additionally, the least-squares algorithm only dictates the acoustic power that a given source must provide, a value that is not equivalent to the electrical power that must be consumed or converted by the source. This section details the process of empirically determining fitting parameters that allow for real sources to be used in the least-squares reconstruction, with the intent of the adjustment parameters being to reduce the reconstruction error.

3.2.1 Effective Impedance

While each source had a reported electrical impedance of 4-8 Ω, it was not known how an applied voltage would translate to a desired pressure at a given distance. Thus, each source was placed at a distance of 1 m from a microphone and supplied 100 mV peak digital voltage from the DAQ. The resultant root-mean-square (RMS) pressure at the microphone was converted to sound power level (L_P):

$$L_P = 10 \log \frac{p_{rms}^2}{p_{ref}^2} = 20 \log \frac{p_{rms}}{p_{ref}} \tag{3.1}$$

with $p_{ref} = 20$ μPa. Still using the assumption of a monopole source with equally radiated power, Eq. (3.2) was used to convert the sound pressure level into a sound power level (L_W):

$$L_W = L_P + 10 \log 4\pi r^2 \approx L_P + 11 + 20 \log r \tag{3.2}$$

where r is expressed in meters. This sound power level was then converted to sound power through the definition

$$L_W = 10 \log \frac{W_{rms}}{W_{ref}} \therefore W_{rms} = W_{ref} 10^{L_W/10} \tag{3.3}$$

with $W_{ref} = 1$ pW. Finally, relating the sound power to the peak input voltage through Joule's First Law and Ohm's Law, an effective coupling impedance Z_{eff} was determined:

$$W_{rms} = \frac{V_{rms}^2}{Z_{eff}} = \frac{V_{pk}^2 G^2}{2 Z_{eff}} \therefore Z_{eff} = \frac{V_{pk}^2 G^2}{2 W_{rms}} \tag{3.4}$$

where G is the gain of the amplifier, a factor of 50 (34 dBV). The impedance of each source was determined at various frequencies, and the values at 7000 Hz, the frequency of most of the following reconstruction tests, are reported in Table 3.1.

Table 3.1.
Effective impedances of sources S0-S7, the sources on the top bar of the array.

Source Number	$\mathbf{Z_{eff}}$ [Ω]
0	13.215
1	15.501
2	9.994
3	16.140
4	17.659
5	23.413
6	14.493
7	14.834

Using these effective impedance values, the acoustic powers of each source as determined by Eq. (2.8) could be translated into peak input voltages to be generated from the DAQ.

3.2.2 Radial Adjustment

Because the tweeters selected did not exhibit perfect monopole behavior, the pressure field around them did not decay exactly with the inverse of the distance from the source. This imperfection was important to consider not just to facilitate reconstruction at variable standoff distances, but also to compensate for the increased distance between sources and receivers that were on opposite sides of the array. The Green's Function for two points (i.e. the source and the receiver) appears in Eq. (2.3) and includes the ideal $1/r$ pressure trend:

$$G = \frac{e^{ikr}}{4\pi r} \tag{3.5}$$

In order to determine the extent of radial correction needed, each source was driven by the appropriate voltage such that the pressure at 1 m would be equal for each source. Measurements of the pressure field were taken from 60 cm to 140 cm away from each source, directly in front of the source. The data were fitted with a least-squares power regression curve, such that $p \propto 1/r^n$. The pressures were normalized to the values at 1 m and are shown in Fig. 3.4.

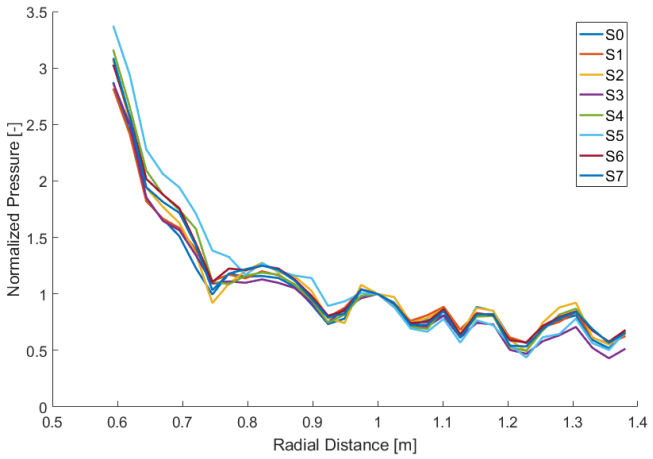

Figure 3.4. A diagram showing the normalized pressure distributions of the sources as a function of distance.

The fitting exponent n was determined by the regression curve for each source, and its values, along with the corresponding coefficient of determination R^2, are presented in Table 3.2.

Table 3.2.
Radial decay exponents of sources S0-S7, the sources on the top bar of the array.

Source Number	n	R^2
0	1.457	0.817
1	1.473	0.867
2	1.481	0.773
3	1.739	0.895
4	1.615	0.812
5	1.953	0.903
6	1.559	0.853
7	1.570	0.832

Note that this empirical correction requires the distance r to be given in meters. Thus, with this adjustment made, the Green's Function becomes

$$\tilde{G} = \frac{e^{ikr}}{4\pi r^n} \tag{3.6}$$

Ultimately, compensating for distance variances is more consequential for the magnitude of the reconstructed pressure wave than for the actual shape. Since the shape of the distribution is more important in the transmission of sound than the magnitude, this adjustment may not be necessary.

3.2.3 Angular Adjustment

Due to the physical construction of the sources and the manner in which they are driven, the sound field at any given distance is not independent of the angle

with respect to the source's axis. In order to determine how much to compensate for these irregularities in pressure, each source was supplied an input voltage to generate a pressure field on a linear arrangement of microphones at a distance of 1 m. As every microphone except for the one on the source's axis was slightly farther than 1 m from the source, the expected pressure field at those microphones was slightly lower. The pressures were normalized to the value at the axial microphone, which would theoretically have the highest value. The normalized pressures, along with the theoretical normalized pressure, can be seen in Fig. 3.5.

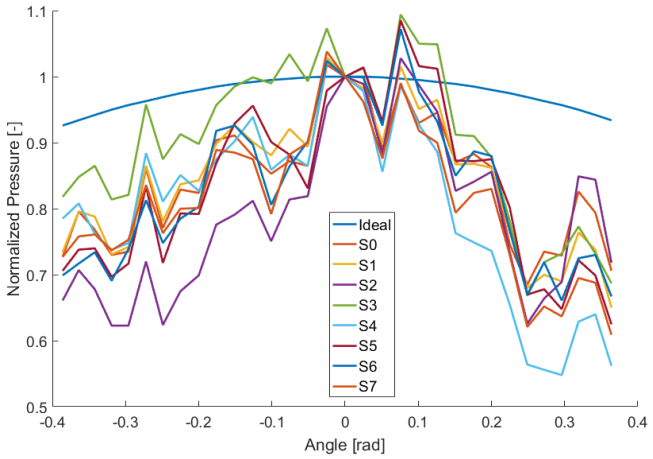

Figure 3.5. A diagram showing the normalized pressure distributions of the sources as a function of angle.

For each source, at each angle, an adjustment factor τ was found by dividing the actual normalized pressure by the expected normalized pressure. By adding this factor to the least-squares algorithm, the modified Green's Function becomes

$$\hat{\tilde{G}} = \tau(\theta)\frac{e^{ikr}}{4\pi r^n} \tag{3.7}$$

The lack of a clear trend in angular pressure distribution may prove to be problematic in the implementation of the least-squares algorithm, as small changes in angle

between a source and a receiver could have significantly different values of τ, leading to inconsistent results.

Both the radial and angular adjustments have the effect of demanding larger source accelerations from sources at large standoffs and angles in an attempt to balance the least-squares algorithm to match the desired pressures. Testing the results of the algorithm both with and without these adjustments will determine if they improve the efficacy of the model.

3.3 Reconstruction Testing Results

An analysis of pressure errors during a preliminary frequency sweep for homogeneous plane wave reconstruction led to a frequency of 7000 Hz being selected for all tests. To minimize the interference between microphones, the spacing of the receiver array was kept at 1 inch (2.54 cm). Sixteen microphones were used, for a total span of 38.1 cm. All of the tests used the 8 tweeters on the top bar of the source array.

In order to account for the physical dimensions of the array components, the default configuration parameters were set at a standoff distance of 1 m, a source spacing of 3 inches (7.62 cm), and the aforementioned design span of 38.1 cm. When the effect of certain parameters was being tested, the other parameters were held at their default values. In the default configuration, the ideal pressure distribution of a 1 Pa homogeneous wave has a maximum pressure error of 18.2×10^{-3} Pa, a RMS pressure error of 6.8×10^{-3} Pa, and demands 17.3 mW of power, as seen in Fig. 3.6.

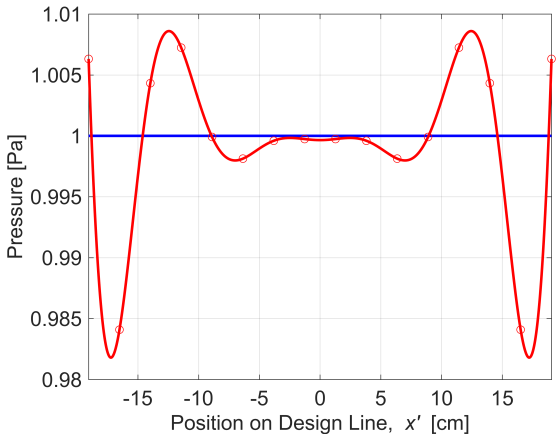

Figure 3.6. A diagram showing the magnitude of the pressure distribution of a reconstructed homogeneous plane wave. The ideal 1 Pa plane wave is shown in blue and the reconstructed wave is shown in red.

By adjusting the standoff distance, source spacing, and inhomogeneity, plots similar to those depicted in Figs. 2.9-2.13 were constructed. The color bar represents the logarithm of the quantity of interest: pressure in pascals and power in watts, respectively. These figures provided the theoretical bounds for all of the tests that were performed. In Fig. 3.7, it can be seen that for the minimum source spacing, approximately 60 cm of standoff distance is required to avoid large errors.

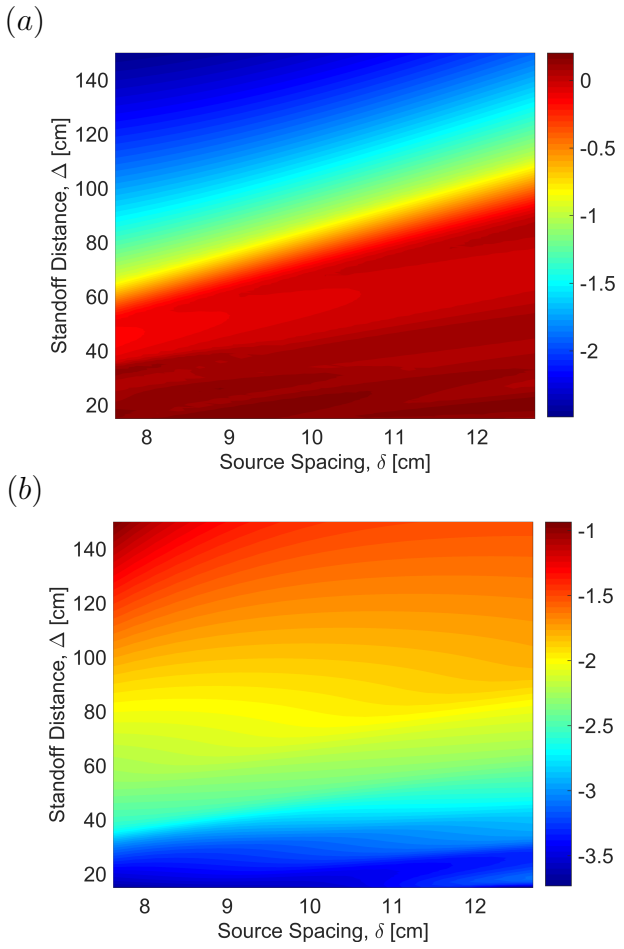

Figure 3.7. A diagram showing the effect of standoff distance and source spacing on (a) the logarithm of the maximum pressure error and (b) the logarithm of the total power consumption.

This is again visible in Fig. 3.8, where it can be seen that inhomogeneity does not have a significant effect on either pressure error or power demand.

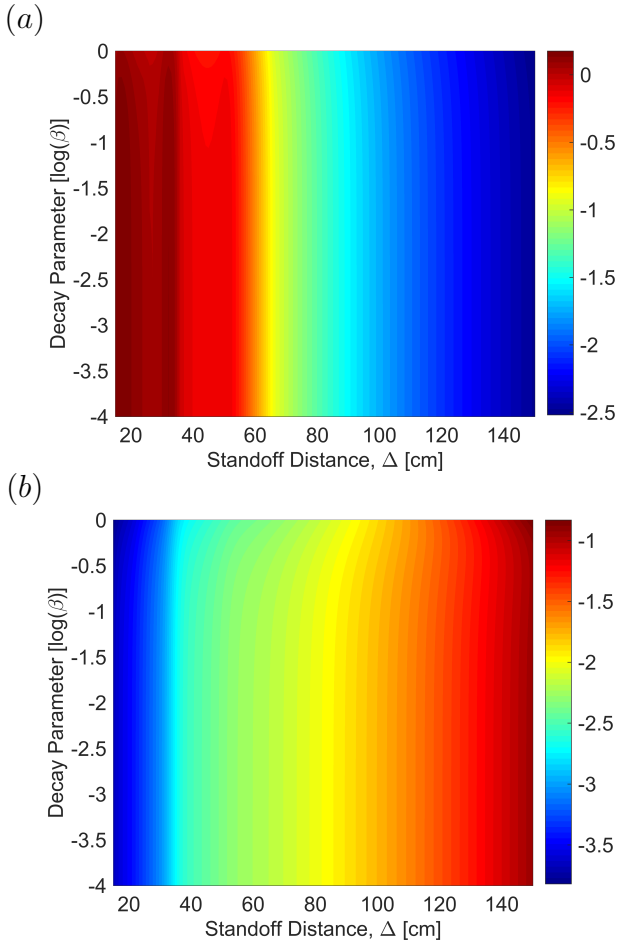

Figure 3.8. A diagram showing the effect of standoff distance and inhomogeneity on (a) the logarithm of the maximum pressure error and (b) the logarithm of the total power consumption.

Errors in pressure generally increase with larger source spacings relative to the design span, and do not depend significantly on inhomogeneity, as seen in Fig. 3.9.

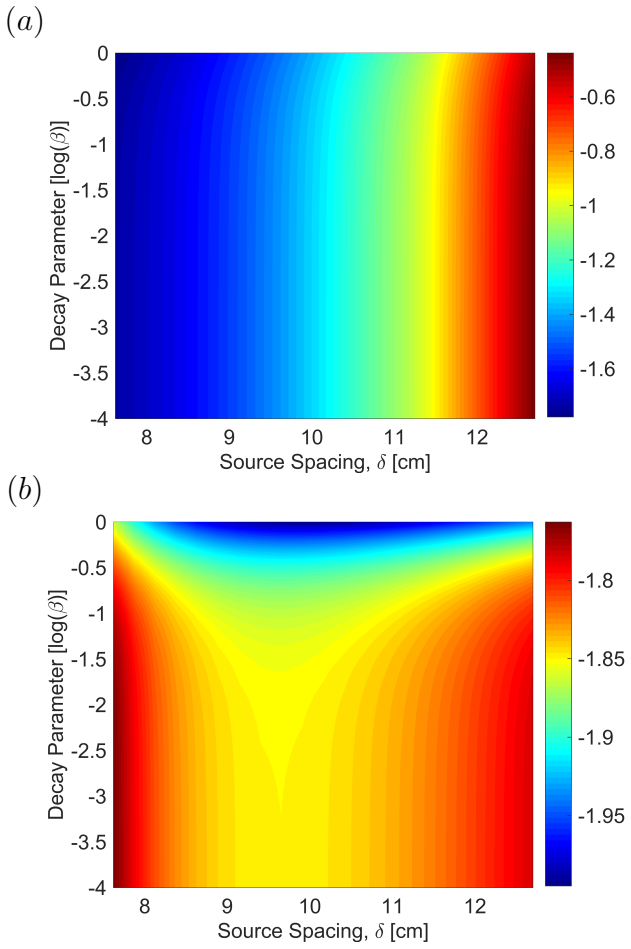

Figure 3.9. A diagram showing the effect of inhomogeneity and source spacing on (a) the logarithm of the maximum pressure error and (b) the logarithm of the total power consumption.

In initial tests, only the impedance of source S0 was found, and the preliminary assumption was made that each source had approximately the same impedance. As is shown in Table 3.1, this is not the case. However, the result of this false assumption was that the radial and angular adjustment factors were able to compensate for the large pressure deviations and ultimately reduce the RMS error. Operating at the minimum source spacing with no inhomogeneity, the standoff distance was varied to evaluate the reconstruction accuracy both with and without the empirical adjust-

ments. At 1 m, the adjustments significantly reduced the RMS error along the design span, as shown in Fig. 3.10.

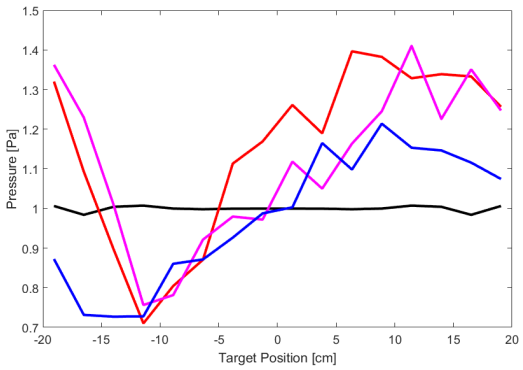

Figure 3.10. A diagram showing the magnitude of the pressure distribution of a reconstructed homogeneous plane wave with no corrections (red), radial corrections (green), and radial and angular corrections (blue) compared with the ideal pressure distribution as given by the least-squares solution (black). The first source's impedance was applied to every source in this model.

Without corrections, the RMS error was 0.26 Pa, but by adding radial and angular adjustments, the error was reduced to 0.16 Pa. Over a range of standoff distances ranging from 0.5 m to 2.0 m, the empirical corrections consistently lowered the RMS error of the reconstructed wave, as shown in Fig. 3.11.

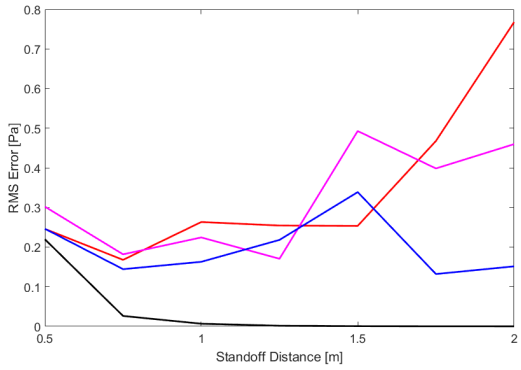

Figure 3.11. A diagram comparing the RMS error of a reconstructed wave at various standoff distances no corrections (red), radial corrections (green), and radial and angular corrections (blue) compared with the ideal pressure distribution as given by the least-squares solution (black).

Over this range of standoff distances, the minimum RMS error was about 0.15 Pa, or 15%, with most of the errors being much higher. At this point, it was hypothesized that finding the impedances of all of the tweeters, not just one, would allow for better reconstruction. Thus, Table 3.1 was formed.

By using these impedances, the test shown in Fig. 3.10 was repeated, with drastically different results. The RMS errors were much lower than when using only one impedance, but the adjustment factors did not serve to improve the reconstruction from the uncorrected trial, as seen in Fig. 3.12.

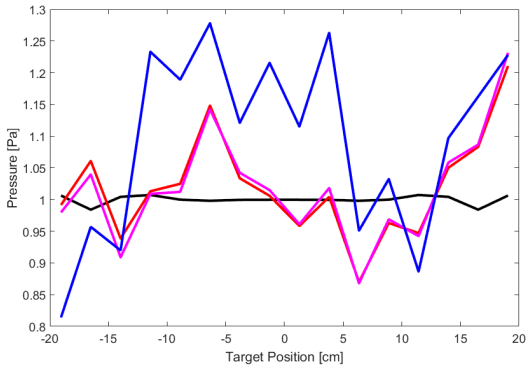

Figure 3.12. A diagram showing the magnitude of the pressure distribution of a reconstructed homogeneous plane wave with no corrections (red), radial corrections (green), and radial and angular corrections (blue) compared with the ideal pressure distribution as given by the least-squares solution (black). Each source's unique impedance was used.

Without any adjustments, the RMS error on the design span was only 0.083 Pa, a reduction of 49% with respect to the previous corrected case. Adding the radial and angular adjustments slightly increased the overall error, though the errors remained below the values yielded by the previous tests. The standoff distance was again varied, and the RMS pressure error at each distance was determined, as seen in Fig. 3.13.

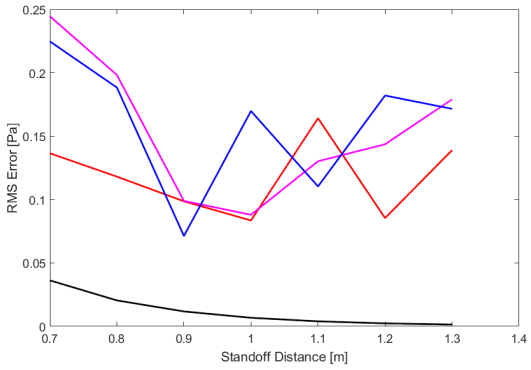

Figure 3.13. A diagram comparing the RMS error of a 1 Pa homogeneous plane wave reconstructed at various standoff distances with no corrections (red), radial corrections (green), and radial and angular corrections (blue) compared with the ideal pressure distribution as given by the least-squares solution (black).

Since the amplitude of the reconstructed wave can ultimately be altered simply through a voltage multiplier, the overall pressure magnitude is less critical to reconstruction than the shape of the wave. By normalizing each reconstructed wave to its mean value along the design span, the RMS errors can be shown to be even smaller, as shown in Fig. 3.14.

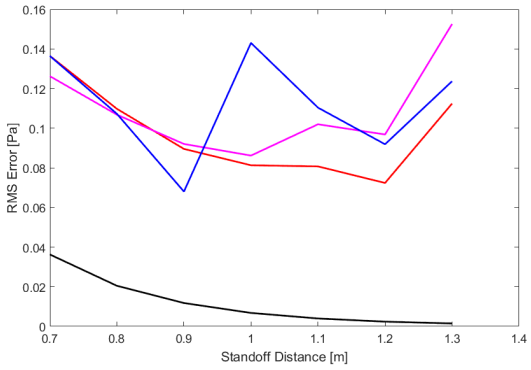

Figure 3.14. A diagram comparing the RMS error of a 1 Pa homogeneous plane wave reconstructed at various standoff distances with no corrections (red), radial corrections (green), and radial and angular corrections (blue) compared with the ideal pressure distribution as given by the least-squares solution (black), normalized to the mean pressure of the wave.

Keeping the standoff distance at 1 m and adjusting the spacing of the tweeters along the span of the source array, the reconstruction tests were repeated. Since increasing the source spacing increased the range of angles between the sources and the microphones but did not significantly increase the distance between them, the angular corrections played a much larger role in these tests. Because only a small range of source spacings yields a small theoretical pressure error, the widest spacing was limited to 10 cm. At this spacing, the radial and angular adjustments test yielded the best result, with the RMS error being 0.10 Pa, compared to the unadjusted test where the RMS error was 0.11 Pa. The adjustments had a very small effect on the overall shape of the wave, but the magnitudes at the design points were much closer to the desired values, as seen in Fig. 3.15.

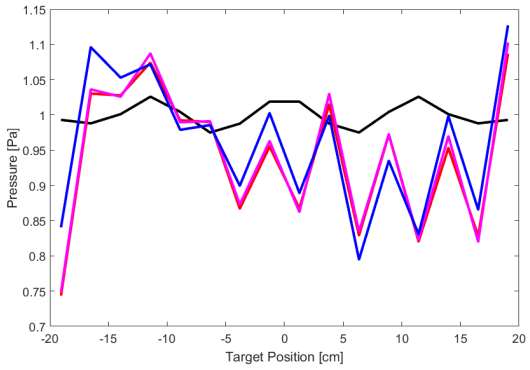

Figure 3.15. A diagram showing the magnitude of the pressure distribution of a reconstructed homogeneous plane wave with no corrections (red), radial corrections (green), and radial and angular corrections (blue) compared with the ideal pressure distribution as given by the least-squares solution (black). Each source's unique impedance was used.

The angular adjustments did not reduce the RMS error at other source spacings, but as was the case with the standoff tests, the errors remained relatively low and did not vary much (Fig. 3.16).

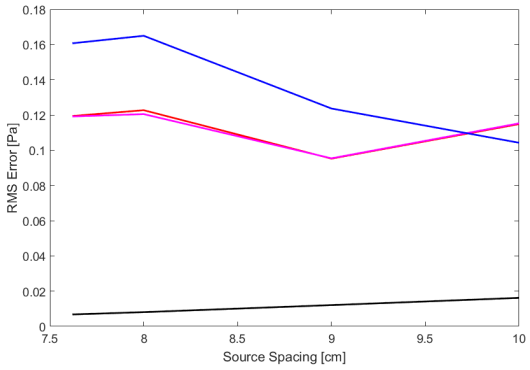

Figure 3.16. A diagram comparing the RMS error of a 1 Pa homogeneous plane wave reconstructed at various source spacings with no corrections (red), radial corrections (green), and radial and angular corrections (blue) compared with the ideal pressure distribution as given by the least-squares solution (black).

Since the mean value of the reconstructed waves was near the desired amplitude, normalizing the errors did not serve to appreciably reduce the errors (Fig. 3.17).

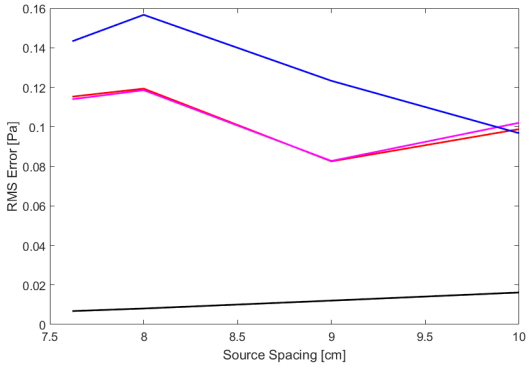

Figure 3.17. A diagram comparing the RMS error of a 1 Pa homogeneous plane wave reconstructed at various source spacings with no corrections (red), radial corrections (green), and radial and angular corrections (blue) compared with the ideal pressure distribution as given by the least-squares solution (black), normalized to the mean pressure of the wave.

To test the reconstruction of an inhomogeneous wave, the desired amplitude on the design span was set as an exponential increase up to 1 Pa. Thus, for a decay parameter of $\beta = 1$ rad/m, the desired distribution was governed by the equation $p = 0.827\mathrm{e}^{x'}$, with x' ranging from -19.05 cm to $+19.05$ cm. For small decay parameters, the inhomogeneous wave appears very similar to a homogeneous wave, and for larger decay parameters, only a small range of the design span requires non-negligible pressures. The largest decay parameter tested, $\beta = 1$ rad/m, saw an improvement in reconstruction with the full set of adjustments (Fig. 3.18). Since the desired amplitude is not constant, the RMS errors are reported as percentages, with the radial and angular corrections yielding an error of 16%.

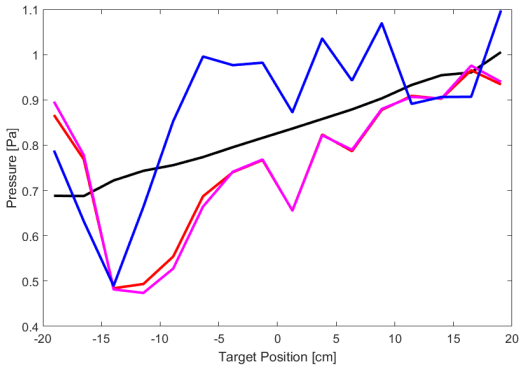

Figure 3.18. A diagram showing the magnitude of the pressure distribution of a reconstructed inhomogeneous plane wave with no corrections (red), radial corrections (green), and radial and angular corrections (blue) compared with the ideal pressure distribution as given by the least-squares solution (black). Each source's unique impedance was used.

While the errors in the uncorrected tests tended to increase with increasing decay parameter, the errors in the radially and angularly corrected tests stayed constant, as seen in Fig. 3.19.

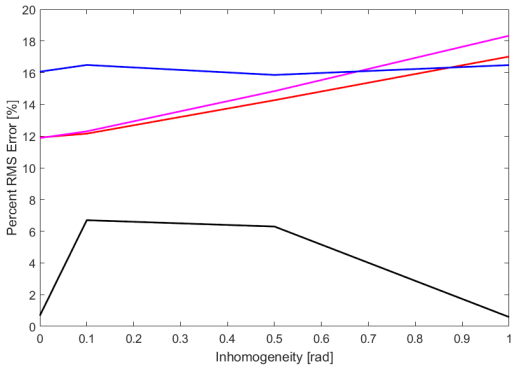

Figure 3.19. A diagram comparing the percent RMS error of a 1 Pa inhomogeneous plane wave reconstructed with various decay parameters with no corrections (red), radial corrections (green), and radial and angular corrections (blue) compared with the ideal pressure distribution as given by the least-squares solution (black).

3.4 Conclusions

Even when attempting to compensate for imperfections in the sources, it was very difficult to significantly reduce the error in the reconstructed plane waves. While adjusting for radial and angular imperfections enhanced the reconstruction of some waves, for some combinations of parameters the adjustments increased the amount of error. This was likely due to the complex nature of the sources, which, despite attempting construction well outside of the near field, had highly variable pressure profiles. A possible solution to this problem would be to operate at lower frequencies, using different sources, although this would place further restrictions on the appropriate dimensions of the arrays. Nevertheless, it is still possible that the current configuration of the acoustic array would be able to generate inhomogeneous waves that are completely transmitted into a solid. While the reconstructed profile might not exactly match the desired profile over the entire design span, the correct decay parameter may appear in localized portions of the target surface, allowing for transmission.

4. FUTURE WORK AND CONCLUSIONS

4.1 Mock Energetic Material Preparation and Preliminary Testing

In anticipation of future tests aiming to excite a mock energetic material, preparations were made for the full utilization of the array. As Sylgard 184 is a common binder material for many types of polymer-based explosives, it was selected as the mock energetic material to be subjected to acoustic excitation. A total of 2.43 kg of Sylgard 184 was mixed and allowed to set in a square frame for 48 hours.

In order to provide a sizeable target area for the source array, and also to allow for a large enough design span should inhomogeneous waves be reconstructed, the Sylgard 184 sample was cast as a square with each side measuring 2 feet (0.61 m). It had a thickness of 1/4 inch (6.35 mm). Twenty reinforced holes with a diameter of 1/4 inch were evenly spaced along the edges to allow for suspension within a metal frame. Fig. 4.1 shows the sample in its mold.

By applying a peak voltage of 100 mV in a digital signal to each of the 32 tweeters, it was estimated that approximately 26.9 W of acoustic power would be generated, leading to a sound power level of 134 dB SWL. The corresponding sound pressure level at a distance of 1 m would be 123 dB SPL, meaning that the pressure at the surface of the sample would be 29.2 Pa. On a target surface of 0.37 m^2, the anticipated average force would be 10.8 N.

Thermal measurements of the surface of the sample were taken using a Forward Looking Infrared (FLIR) C3 Pocket Thermal Camera, placed 75 cm behind the source array. The sample was placed in the sound field for a period of 30 minutes, with thermal images being taken every minute. A microphone was placed at the top of the sample to verify the pressure present near the surface. The sample itself

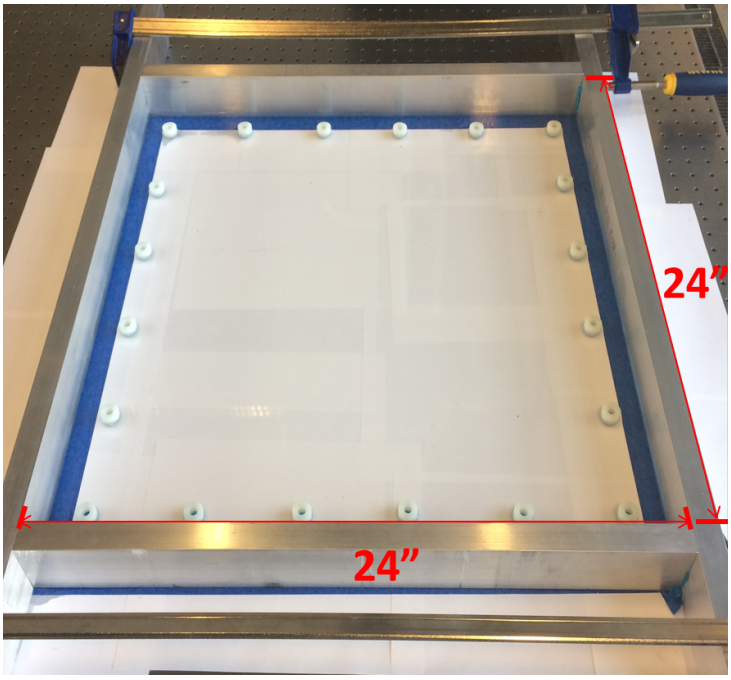

Figure 4.1. A diagram showing the Sylgard 184 sample in its mold.

Figure 4.2. A diagram showing the Sylgard 184 sample suspended in its frame.

was suspended within its stand using lightly tensioned bungee cords to ensure that significant lateral movement would not occur, as shown in Fig. 4.2.

The source array was positioned at a distance of 1 m from the sample such that the sample was normal to the incident pressure waves. The full experimental setup is shown in Fig. 4.3.

Solving Eq. (1.15) using the longitudinal and shear wave speeds for Sylgard 184, the Rayleigh wave speed can be found to be 530 m/s. As stated in Chapter 1, the corresponding Rayleigh angle is 40.32°. While the magnitude of the reflection coefficient is in fact minimized at this angle of incidence, for all practical purposes, it is still approximately equal to unity, as seen in Fig. 4.4a. The ordinate of Fig. 4.4a is $1 - |R|$ to illustrate the very small departure from unity. To reduce the reflection coefficient to zero, inhomogeneity must be introduced into the incident wave. The optimum decay parameter scales linearly with frequency, so at 7000 Hz, β takes a value of 0.01505 rad/m. As seen in Fig. 4.4b, at the Rayleigh angle, the incident inhomogeneous wave is completely transmitted.

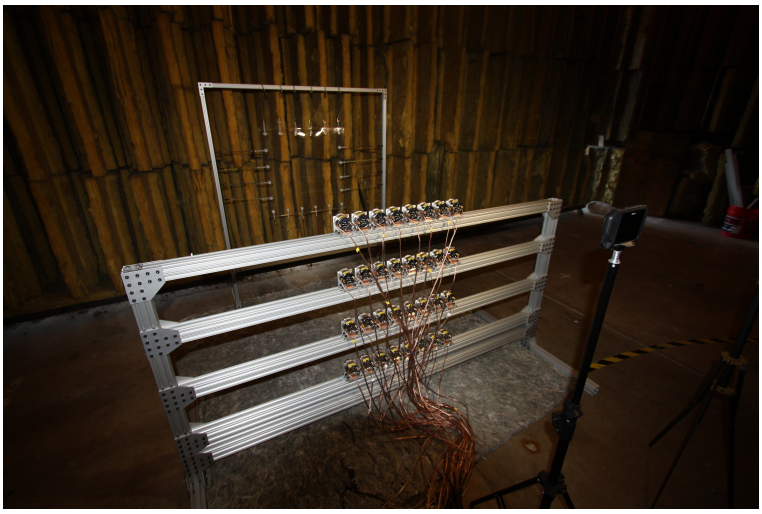

Figure 4.3. A diagram showing the experimental setup of the source array, Sylgard 184 sample, and FLIR camera.

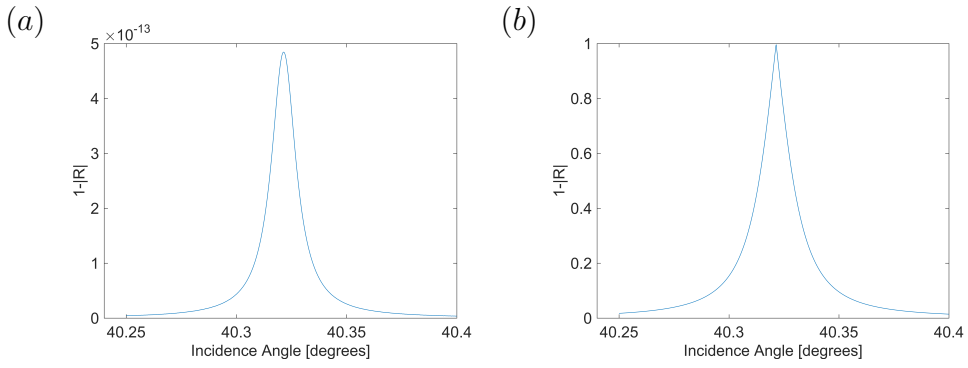

Figure 4.4. A diagram showing the departure from unity of the magnitude of the pressure reflection coefficient for an incident wave with (a) $\beta = 0$ rad/m and (b) $\beta = 0.01505$ rad/m.

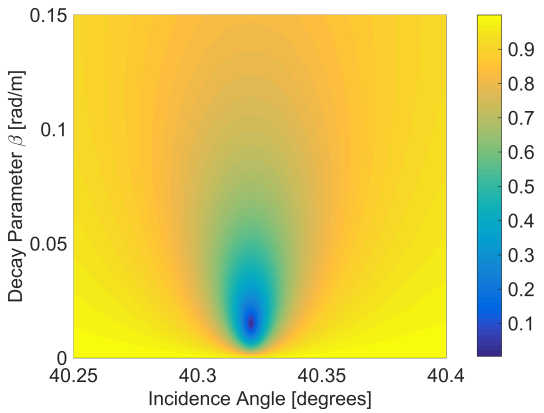

Figure 4.5. A diagram showing the minimization of the pressure reflection coefficient of a 7000 Hz inhomogeneous plane wave incident on Sylgard 184.

By finding the reflection coefficient at various decay parameters and incidence angles, Fig. 1.8 can be reproduced for a 7000 Hz wave, as seen in Fig. 4.5.

Since the optimum decay parameter is very small, the incident wave would appear almost as a homogeneous wave. As was shown in Chapter 3, errors in the reconstruction process would render such an inhomogeneous wave as almost indistinguishable from a homogeneous wave. As such, surface temperature and vibration tests will focus on the transmission of acoustic energy without respect to the exact form of the incident wave.

Tests were performed with the sample positioned at normal incidence and also angled at 40.32°, the Rayleigh angle. Thermal imaging was used to identify the hottest spot near the middle of the sample.

In the normal incidence test, the measured sound pressure level was approximately 111 dB, significantly less than the predicted 123 dB. This is likely due to the fact that the measurement was taken at the top of the sample rather than at the point directly across from the center of the source array. At this pressure level, the particle velocity is approximately 17 mm/s and is conserved across the interface. Despite the sources

receiving the same input voltage for the Rayleigh angle test, the sound pressure level increased to 117 dB, with a normal particle velocity of about 26 mm/s. While the absolute position of the microphone did not change between the two tests, reflections from the sample itself likely contributed to this rise in pressure level.

The maximum temperature trends over the course of the tests are plotted in Fig. 4.6.

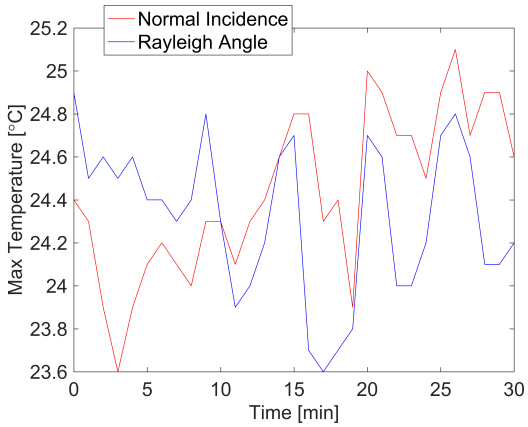

Figure 4.6. A diagram showing the maximum temperature of the Sylgard 184 sample when subjected to acoustic excitation at normal incidence and at the Rayleigh angle.

While the maximum temperature tended to increase during the normal incidence test and tended to decrease during the Rayleigh angle test, the magnitude of these changes was very small. By examining the thermal images of the sample (Fig. 4.7), it can be seen that while the temperature of the sample varied, so did the temperature of the surroundings. This suggests that the thermomechanical effect of the acoustic excitation is negligible compared to the effect of airflow in the environment.

Additionally, despite the high pressures at the surface of the sample, no lateral motion was observed. It is possible that surface vibrations were so small and occurring at such a high frequency that they were not visible to the unaided eye. Future work will utilize a laser Doppler vibrometer to determine the extent to which vibra-

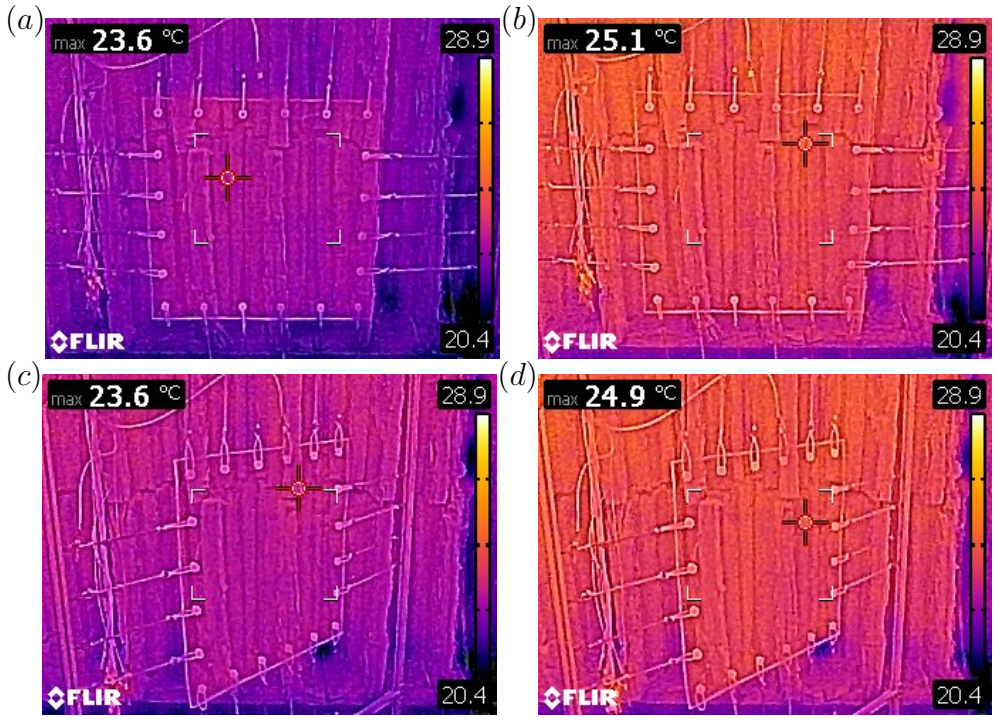

Figure 4.7. A diagram showing the lowest and highest maximum temperatures recorded on the Sylgard 184 sample at (a)-(b) normal incidence and (c)-(d) the Rayleigh angle.

tions are induced on the surface of the sample. Direct-contact mechanical testing of mock energetic materials has shown that low-frequency excitations lead to appreciable particle velocities on the materials' surfaces. For example, when a cylinder of sucrose-loaded mock energetic material was excited near its resonance at 11.41 kHz for a period of 15 minutes, the particle velocity at the surface was calculated to be about 65 mm/s, slightly higher than the estimated velocities from the acoustics tests. This direct-contact excitation yielded a maximum temperature increase of 12 °C on the top surface of the cylinder [35]. In order to induce higher surface velocities and therefore higher heating rates, higher acoustic pressures will be required, which will mean either reducing the standoff distance or increasing the source powers.

4.2 Future Work

Future work in the area of energetic material detection will be largely two-fold: modeling the sources and transmitting energy into the material. In order to reconstruct a sound field more accurately, the properties of the sources must be well understood. In the context of the work discussed in Chapter 3, this could mean either replacing the current sources with a more consistent type of speaker, or developing a more universal model of the current sources. Sources designed for low-frequency outputs would likely exhibit a more monopole-like pressure distribution, but they would likely be larger in size, limiting the parameter of source spacing. If the current sources are used, a more complex model could be utilized to determine their properties through the use of the least-squares method itself. Prior work has suggested that any complex sound source can be modeled as the superposition of multiple simple sources, like monopoles, dipoles, and quadrupoles [36, 37]. By taking sound pressure measurements at several locations in space in front of a given source, applying the least-squares algorithm with the appropriate Green's Functions, and treating each source as a combination of other sources, a more comprehensive model could be de-

veloped. This model would take the place of the modified Green's Function as given by Eq. (3.6).

While the analysis of transmission discussed in Chapter 1 assumes a lossless solid medium, all materials ultimately have some level of dissipation, generally through hysteretic damping [13]. This leads to the attenuation of any transmitted wave along the direction of propagation. For a homogeneous wave, the attenuation vector is in the same direction as the propagation vector, but for an inhomogeneous wave, which already exhibits attenuation perpendicular to propagation, the attenuation vector bends towards the propagation vector. The difference between the propagation angle and the attenuation angle is known as the degree of inhomogeneity. Damping in the target material ultimately causes the optimum decay parameter for transmission to change slightly, but the optimum incidence angle remains the Rayleigh angle. By knowing the Lamé parameters of the target material in question, the complex longitudinal and shear wavenumbers can be found, leading to the calculation of the decay parameter that will minimize reflection at the Rayleigh angle [13]. The material properties of Sylgard 184 will need to be studied more comprehensively in order to fully incorporate the effect of dissipation into the model of transmission. As previously mentioned, the response of a material to an inhomogeneous wave will be recorded using an infrared camera to measure temperature variance and a laser Doppler vibrometer to measure surface velocity.

4.3 Overall Conclusions

As many current methods of energetic material detection are ineffective or dangerous, there exists a need to provide a reliable, easily implementable procedure for exciting and identifying these materials. The most promising of potential excitation methods is that of acoustic perturbation, where specially tailored waves are able to bridge the impedance gap between the energetic material and the surrounding air. The result is the full transmission of acoustic energy into mechanical energy, and ul-

timately heat that increases the temperature of the material. A temperature increase corresponds to a vapor pressure increase, which in turn allows for the identification of the energetic material through a trace vapor detection probe.

The least-squares method of sound field reconstruction was shown to be a powerful tool in allowing for the design of specialized inhomogeneous pressure waves at a prescribed standoff distance. In simulations utilizing perfect monopole sources, it was shown that 8 sources were able to reconstruct a desired pressure field with minimal errors and power consumption, provided that a sufficient standoff distance was chosen. Because spherical waves appear similar to plane waves at large distances from their sources, pressure errors are minimized at large standoff distances. However, this comes at the cost of an increased demand in power, as the intensity of a wave decreases with the inverse of the distance squared. Inhomogeneous plane waves can be reconstructed with the same level of accuracy as homogeneous plane waves, but could cause larger relative errors at locations where the desired pressure amplitude is very low. Small deviations in the prescribed source powers or phases could lead to noticeable errors in the reconstructed wave, so care must be taken to ensure that the source positions and outputs are as close to the model as possible.

When implementing least-squares reconstruction utilizing real sources, it became important to characterize each source based on its response to system inputs. By relating the applied voltage to the acoustic power dissipated by each source, an effective impedance was formulated. While in many cases, this effective impedance was sufficient to enable the least-squares model to generate pressure profiles with low levels of error, some tests required empirical adjustments based on the imperfections of the source in order to keep the pressure errors low. However, due to irregularities in the sources, it was not possible to reduce the pressure error to the values predicted by the least-squares model.

Using the full source array of 32 tweeters generating a 7000 Hz wave, a panel of the mock energetic binder Sylgard 184 was subjected to pressure levels of over 111 dB. At both normal incidence and the Rayleigh angle, no appreciable temperature

change was observed, confirming the principle that untuned acoustic waves are not able to easily transmit energy across the fluid–solid interface. However, by using more precise sources and models in the future, it should be possible to reconstruct waves with sufficient accuracy to induce thermomechanical excitations in energetic materials.

REFERENCES

REFERENCES

[1] T. A. Kyle, D. C. Woods, J. S. Bolton, and J. F. Rhoads, "Least-squares reconstruction of low-frequency inhomogeneous plane waves," *Journal of Sound and Vibration*, Submitted, 2018.

[2] F. L. Becker and R. L. Richardson, "Influence of material properties on Rayleigh critical-angle reflectivity," *Journal of the Acoustical Society of America*, 51(5B):1609–1617, 1972.

[3] S. Meyer, S. A. Hindle, J. P. Sandoz, T. H. Gan, and D. A. Hutchins, "Non-contact evaluation of milk-based products using air-coupled ultrasound," *Measurement Science and Technology*, 17(7):1838–1846, 2006.

[4] A. V. Kuznetsov and O. I. Osetrov, "Detection of improvised explosives (IE) and explosive devices (IED)," *Detection and Disposal of Improvised Explosives, NATO Security through Science Series B: Physics and Biophysics*, pp. 7–25, 2006.

[5] J. Otto, M. F. Brown, and W. Long, "Training rats to search and alert on contraband odors," *Applied Animal Behaviour Science*, 77(3):217–232, 2002.

[6] A. Gordin and A. Amirav, "SnifProbe: New method and device for vapor and gas sampling," *Journal of Chromatography A*, 903(1):155–172, 2000.

[7] H. Östmark, S. Wallin, and H. G. Ang, "Vapor pressure of explosives: A critical review," *Propellants, Explosives, Pyrotechnics*, 37(1):12–23, 2012.

[8] M. A. Biot, "Linear thermodynamics and the mechanics of solids," in *Proceedings of the Third U.S. National Congress of Applied Mechanics, Providence, RI, USA*, pp. 1–18, 1958.

[9] L. E. Kinsler, A. R. Frey, A. B. Coppens, and J. V. Sanders, *Fundamentals of Acoustics*. John Wiley & Sons, 1999.

[10] L. M. Brekhovskikh, *Waves in Layered Media*. Academic Press, 1960.

[11] P. M. Morse and K. U. Ingard, *Theoretical Acoustics*. McGraw-Hill, 1968.

[12] D. C. Woods, J. S. Bolton, and J. F. Rhoads, "On the use of evanescent plane waves for low-frequency energy transmission across material interfaces," *Journal of the Acoustical Society of America*, 138(4):2062–2078, 2015.

[13] D. C. Woods, J. S. Bolton, and J. F. Rhoads, "Enhanced acoustic transmission into dissipative solid materials through the use of inhomogeneous plane waves," *Journal of Physics: Conference Series*, 744(1):012188, 2016.

[14] R. D. Borcherdt, *Viscoelastic Waves in Layered Media*. Cambridge University Press, 2009.

[15] J. C. F. Millett, G. Whiteman, S. M. Stirk, and N. K. Bourne, "Shear strength measurements in a shock loaded commercial silastomer," *Journal of Physics D: Applied Physics*, 44(18):185403, 2011.

[16] H. L. Bertoni and T. Tamir, "Unified theory of Rayleigh-angle phenomena for acoustic beams at liquid–solid interfaces," *Applied Physics*, 2(4):157–172, 1973.

[17] J. D. N. Cheeke, *Fundamentals and Applications of Ultrasonic Waves*. CRC Press, 2012.

[18] J. W. Strutt, "On waves propagated along the plane surface of an elastic solid," in *Proceedings of the London Mathematical Society*, 17(1):4–11, 1885.

[19] S. Vanaverbeke, F. Windels, and O. Leroy, "The reflection of bounded inhomogeneous waves on a liquid/solid interface," *Journal of the Acoustical Society of America*, 113(1):73–83, 2003.

[20] D. C. Woods, J. S. Bolton, and J. F. Rhoads, "Bounded inhomogeneous wave profiles for increased surface wave excitation efficiency at fluid–solid interfaces," *Journal of the Acoustical Society of America*, 141(4):2779–2787, 2017.

[21] H. Cox, R. Zeskind, and M. Owen, "Robust adaptive beamforming," *IEEE Transactions on Acoustics, Speech, and Signal Processing*, 35(10):1365–1376, 1987.

[22] B. D. Van Veen and K. M. Buckley, "Beamforming: A versatile approach to spatial filtering," *IEEE ASSP Magazine*, 5(2):4–24, 1988.

[23] O. Kirkeby and P. A. Nelson, "Reproduction of plane wave sound fields," *Journal of the Acoustical Society of America*, 94(5):2992–3000, 1993.

[24] A. J. Berkhout, D. de Vries, and P. Vogel, "Acoustic control by wave field synthesis," *Journal of the Acoustical Society of America*, 93(5):2764–2778, 1993.

[25] J. Ahrens and S. Spors, "Sound field reproduction using planar and linear arrays of loudspeakers," *IEEE Transactions on Audio, Speech, and Language Processing*, 18(8):2038-2050, 2010.

[26] H. Itou, K. Furuya, and Y. Haneda, "Evanescent wave reproduction using linear array of loudspeakers," in *Proceedings of the IEEE Workshop on Applications of Signal Processing to Audio and Acoustics, New Paltz, NY, USA*, pp. 37–40, 2011.

[27] J. Ahrens, M. R. Thomas, and I. Tashev, "Efficient implementation of the spectral division method for arbitrary virtual sound fields," in *Proceedings of the IEEE Workshop on Applications of Signal Processing to Audio and Acoustics, New Paltz, NY, USA*, pp. 1–4, 2013.

[28] O. Robin, A. Berry, and S. Moreau, "Experimental vibroacoustic testing of plane panels using synthesized random pressure fields," *Journal of the Acoustical Society of America*, 135(6):3434–3445, 2014.

[29] D. Trivett, L. Luker, S. Petrie, A. Van Buren, and J. Blue, "A planar array for the generation of evanescent waves," *Journal of the Acoustical Society of America*, 87(6):2535–2540, 1990.

[30] T. J. Matula and P. L. Marston, "Electromagnetic acoustic wave transducer for the generation of acoustic evanescent waves on membranes and optical and capacitor wave-number selective detectors," *Journal of the Acoustical Society of America*, 93(4):2221–2227, 1993.

[31] M. Deschamps, "Reflection and refraction of the evanescent plane wave on plane interfaces," *Journal of the Acoustical Society of America*, 96(5):2841–2848, 1994.

[32] A. Fujii, N. Wakatsuki, and K. Mizutani, "A planar acoustic transducer for near field acoustic communication using evanescent wave," *Japanese Journal of Applied Physics*, 53(7):07KB07, 2014.

[33] D. A. Russell, J. P. Titlow, and Y. Bemmen, "Acoustic monopoles, dipoles, and quadrupoles: An experiment revisited," *Journal of the Acoustical Society of America*, 67(8):660–664, 1999.

[34] D. C. Woods, "On the use of mechanical and acoustical excitations for selective heat generation in polymer-bonded energetic materials," *ProQuest Dissertations Publishing*, 10245773, 2016.

[35] A. R. Range, personal communication, April 24, 2018.

[36] R. Madoliat, N. M. Nouri, and A. Rahrovi, "Developing general acoustic model for noise sources and parameters estimation," *American Institute of Physics*, 7(2):025014, 2017.

[37] Y. Liu and J. S. Bolton, "The use of non-collocated higher order sources in the equivalent source method," *InterNoise12 Proceedings*, 12(8):7326–7337, 2012.